Hot and counter-rotating star-forming disc galaxies in IllustrisTNG and their real-world counterparts

MNRAS 000, 1–18 (2020) Preprint 18 February 2021 Compiled using MNRAS LATEX style file v3.0

Hot and counter-rotating star-forming disk galaxies in IllustrisTNG and their real-world counterparts

Shengdong Lu[1]★, Dandan Xu[1]†, Yunchong Wang[2], Yanmei Chen[3], Ling Zhu[4], Shude Mao[1], Volker Springel[5], Jing Wang[6], Mark Vogelsberger[7], Lars Hernquist[8]

[1]*Department of Astronomy, Tsinghua University, Beijing 100084, China*
[2]*Kavli Institute for Particle Astrophysics and Cosmology, Physics Department, Stanford University, Stanford, CA 94305*
[3]*Department of Astronomy, Nanjing University, Nanjing, China*
[4]*Shanghai Astronomical Observatory, Chinese Academy of Sciences, 80 Nandan Road, Shanghai 200030, China*
[5]*Max-Planck-Institut für Astrophysik, Karl-Schwarzschild-Str. 1, D-85748, Garching, Germany*
[6]*Kavli Institute for Astronomy and Astrophysics, Peking University, Beijing 100871, China*
[7]*Kavli Institute for Astrophysics and Space Research, Department of Physics, MIT, Cambridge, MA 02139, USA*
[8]*Harvard-Smithsonian Center for Astrophysics, 60 Garden Street, Cambridge, MA 02138, USA*

Accepted ***. Received ***; in original form ***

ABSTRACT

A key feature of a large population of low-mass, late-type disk galaxies are star-forming disks with exponential light distributions. They are typically also associated with thin and flat morphologies, blue colours, and dynamically cold stars moving along circular orbits within co-planar thin gas disks. However, the latter features do not necessarily always imply the former, in fact, a variety of different kinematic configurations do exist. In this work, we use the cosmological hydrodynamical IllustrisTNG Simulation to study the nature and origin of dynamically hot, sometimes even counter-rotating, star-forming disk galaxies in the lower stellar mass range (between $5 \times 10^9\,\mathrm{M}_\odot$ and $2 \times 10^{10}\,\mathrm{M}_\odot$). We find that being dynamically hot arises in most cases as an induced transient state, for example due to galaxy interactions and merger activities, rather than as an age-dependent evolutionary phase of star-forming disk galaxies. The dynamically hot but still actively star-forming disks show a common feature of hosting kinematically misaligned gas and stellar disks, and centrally concentrated on-going star formation. The former is often accompanied by disturbed gas morphologies, while the latter is reflected in low gas and stellar spins in comparison to their dynamically cold, normal disk counterparts. Interestingly, observed galaxies from MaNGA with kinematic misalignment between gas and stars show remarkably similar general properties as the IllustrisTNG galaxies, and therefore are plausible real-world counterparts. In turn, this allows us to make predictions for the stellar orbits and gas properties of these misaligned galaxies.

Key words: galaxies: formation – galaxy: evolution – galaxy: kinematics and dynamics – methods: numerical

1 INTRODUCTION

Star-forming disk galaxies with exponential surface brightness profiles are often associated with thin and flat morphologies, blue colours, and dynamically cold stars moving along circular orbits within the co-planar thin gas disks. This is a standard picture inherited from the disk formation theory, which posits that a proto dark-matter halo gains its initial angular momentum through interactions with its surrounding gravitational tidal fields until turnaround (Hoyle 1949; Peebles 1969; Doroshkevich 1970; Fall 1983; White 1984; Catelan & Theuns 1996), after which the subsequent virialization preserves angular momentum, and the gas settles into a rotation-supported disk with size related to spin (Fall & Efstathiou 1980; Mo et al. 1998) as it radiatively cools down and accretes towards the halo center (e.g. Kereš et al. 2005; Dekel & Birnboim 2006), Correspondingly, subsequent generations of stars that form inside the rotating gaseous disk naturally inherit a tangential motion and in this way build up a flat and dynamically cold disk component of the galaxy (e.g. Zavala et al. 2015).

Recent hydrodynamic simulations have allowed us to follow the detailed evolution of galaxies during the non-linear growth era,

★ E-mail: lushengdong@tsinghua.edu.cn
† E-mail: dandanxu@tsinghua.edu.cn

and have shown that various processes complicate the simple picture described above (e.g. Zavala et al. 2015; Zjupa & Springel 2017 and references therein): angular momenta can be lost and regained due to galactic winds and accretion, can be transferred between dark matter, gas and stars, can be redistributed from one part of the galactic halo to the other, or be modified by merger processes. As a consequence, galaxies can transform between different morphologies and kinematics while varying their star-forming activities accordingly. It is not entirely clear how a dynamically cold star-forming disk galaxy starts getting heated up and becomes dynamically hot, eventually ceasing its star-formation and acquiring a spheroidal/elliptical shape. This process is likely to proceed along multiple paths under different circumstances.

In Xu et al. (2019), the luminosity/stellar contributions of different dynamical components (in terms of orbit circularity) were calculated for galaxies from one of the currently most advanced cosmological hydrodynamic models – the IllustrisTNG Simulation (Marinacci et al. 2018; Naiman et al. 2018; Nelson et al. 2018; Pillepich et al. 2018; Springel et al. 2018), which was compared to a sample of 260 CALIFA galaxies (Falcón-Barroso et al. 2017; Zhu et al. 2018), showing general agreement in many properties. Interestingly, a fraction of the simulated lower-mass, late-type galaxies (within a stellar mass range between $5 \times 10^9\,\mathrm{M}_\odot$ and $2 \times 10^{10}\,\mathrm{M}_\odot$) with active star-formation and exponential light profiles (i.e., disk-dominated morphologies), exhibited however fairly high (low) fractions of dynamically hot (cold) stellar orbits. From the observational perspective, this has also been seen in star-forming galaxies within this mass range. For example, in Zhu et al. (2018), some of the lower-mass and star-forming CALIFA galaxies indeed have relatively low cold orbit fraction but higher hot orbital fraction – a feature not fully compatible with usual disk-dominated galaxies.

In this study, we investigate the nature and origin of these objects further using the IllustrisTNG Simulation. We find that these systems show a common feature of hosting kinematically misaligned gas and stellar disks, as well as centrally-concentrated on-going star formation. The former is often accompanied by disturbed gas morphologies to a certain extent, whereas the latter is consistent with low gas and stellar spins. In comparison, their dynamically cold star-forming disk counterparts exhibit well-established and co-planar gaseous disks and extended on-going star-forming activity.

Indeed, various forms of misalignments have been widely reported in these systems, between gas and stars, as well as between morphology and kinematics. An extreme case is when the spin of the gas disk lies in completely the opposite direction to that of existing stars, which is dynamically more stable than a misalignment at any other angles (Hunter & Toomre 1969; Tohline & Durisen 1982). Under such circumstances, the current in-situ star-formation naturally results in the youngest stellar population inheriting the gas orbital motion, and thus moving against the bulk spin dominated by the older stellar population; the galaxy can thus also possess a good fraction of counter-rotating stellar orbits (e.g. Algorry et al. 2014; Starkenburg et al. 2019). Such a dynamically mixed configuration can be unveiled more specifically by conducting an orbit-based modeling (e.g. Zhu et al. 2018). Large misalignment between the kinematic axes of gas and stars or counter-rotation among different stellar components are also smoking gun signatures for such a system and can be easily recognized from the velocity maps of galaxies (e.g., Coccato et al. 2013, 2015; Katkov et al. 2016; Pizzella et al. 2018; Li et al. 2021).

Throughout the years, the origin of such misalignments has been suggested to be related to galaxy mergers (e.g. Balcells & Stanford 1990; Hernquist & Barnes 1991; Barnes & Hernquist 1996; Crocker et al. 2009), satellite accretion (e.g. Thakar & Ryden 1996; Puerari & Pfenniger 2001; Algorry et al. 2014), or misaligned gas accretion (e.g. Pizzella et al. 2004; Roškar et al. 2010; van de Voort et al. 2015; Graham et al. 2017; Starkenburg et al. 2019; Khoperskov et al. 2021), which are not necessarily exclusive to one another.

In this study, we find evidence that the dynamically hot configurations are often linked to recent galactic interactions and mergers, which trigger a subsequent misalignment between the spins of gas and stars in the inner regions of galaxies. Our study also reveals that being dynamically hot is typically a transient state rather than a long-term evolutionary phase for star-forming disk galaxies. Interestingly, such an "unfortunate" disk galaxy is also able to get "healthy" again. Through our comparison, remarkable similarities in the distributions of many observational properties are found between misaligned star-forming galaxies from the MaNGA survey and the dynamically hot star-forming disks from the IllustrisTNG Simulation.

The paper is organized as follows. In Section 2, we introduce how we calculate relevant properties for galaxies from the IllustrisTNG Simulation (Section. 2.1), and how we select sample galaxies for this study (Section 2.2). In Section 3, we present how typical dynamically hot star-forming disks look like, considering their stellar and gas components, their morphologies (Section 3.1), kinematics (Section 3.2), and star-formation activities (Section 3.3). In Section 4, we discuss the formation and evolution of dynamically hot star-forming disk galaxies in comparison to their normal disk counterparts. In Section 5, we present several key observational properties of the real-world counterparts to the simulated galaxies for comparison. In particular, predictions are made for the misaligned galaxies with respect to stellar-orbit and gas observations. Finally, conclusions and some further discussions are given in Section 6.

In this work, we adopt the cosmology used in the IllustrisTNG simulation, which is based on results of the Planck experiment (Planck Collaboration et al. 2016): flat universe geometry is assumed with a total matter density of $\Omega_\mathrm{m} = 0.3089$ (with a baryonic density of $\Omega_\mathrm{b} = 0.0486$), a cosmological constant of $\Omega_\Lambda = 0.6911$, and a Hubble constant $h = H_0/(100\,\mathrm{km s^{-1} Mpc^{-1}}) = 0.6774$.

2 METHODOLOGY

The Next Generation Illustris Simulations (IllustrisTNG, TNG hereafter; Marinacci et al. 2018; Naiman et al. 2018; Nelson et al. 2018, 2019b; Pillepich et al. 2018, 2019; Springel et al. 2018) are a suite of state-of-the-art magneto-hydrodynamic cosmological galaxy formation simulations carried out in large cosmological volumes with the moving-mesh code AREPO (Springel 2010). In this study, we use the full-physics version with a cubic box of 110.7 Mpc side length (TNG100), which has a mass resolution for baryonic and dark matter of $m_\mathrm{baryon} = 1.4 \times 10^6\,\mathrm{M}_\odot$ and $m_\mathrm{DM} = 7.5 \times 10^6\,\mathrm{M}_\odot$, respectively. The gravitational softening length for dark matter and stellar particles is $\epsilon_\mathrm{softening} = 0.74$ kpc. Galaxies in their host dark matter halos are identified using the SUBFIND algorithm (Springel et al. 2001; Dolag et al. 2009). General galaxy properties have been calculated and publicly released by the TNG collaboration[1] (Nelson et al. 2019a). In the following, we explain how several specific further galaxy properties are calculated, and how three key galaxy samples are composed for this study.

[1] http://www.tng-project.org/data/

2.1 Galaxy property calculation

Star-formation rate, morphology and kinematics are three main aspects describing the state of a given galaxy. Below we detail the definition of a few further galaxy properties that we calculate using the constituent particle/cell information:

(i) specific star-formation rate sSFR in the past 1 Gyr, calculated within a 2D aperture of radius $2R_{\rm hsm}$, where $R_{\rm hsm}$ is the 3D half-stellar mass radius measured from the center of a given galaxy.

(ii) a bulge-to-total luminosity ratio $L_{\rm dev}/L_{\rm tot}$, given by the de Vaucouleurs (de Vaucouleurs 1948) to total luminosity ratio, which is obtained from fitting a two component model composed of a de Vaucouleurs and an exponential profile to the radial surface brightness distribution of the elliptical isophotes (see Xu et al. 2017 for details).

(iii) the surface stellar mass density calculated within an aperture of radius $R_{\rm hsm}$, $\Sigma_{*,R_{\rm hsm}}$.

(iv) the shortest-to-longest axis ratios $(c/a)_*$ and $(c/a)_{\rm gas}$ of a galaxy's stellar and gaseous disks, respectively, obtained through finding eigenvectors of the associated inertia tensors (Allgood et al. 2006), defined using particles/cells within a chosen 3D radius from the galaxy center. This radius is set to be the smaller one of $3R_{\rm hsm}$ and 30 kpc, in order to restrict the calculation to the visible galaxy region.

(v) the stellar and HI gas (here the HI gas refers to neutral hydrogen, without distinguishing molecular hydrogen and atomic hydrogen) line-of-sight velocity maps within a square of $[-3R_{\rm hsm}, 3R_{\rm hsm}]^2$ from the galaxy center in a given projection, weighted by stellar luminosity and HI mass, respectively.

(vi) spin parameters: specific angular momenta for both stellar (j_*) and gaseous ($j_{\rm gas}$) components calculated within $3R_{\rm hsm}$.

(vii) luminosity fractions of stars in "cold", "hot" and "counter-rotating cold" orbits. An orbital type is defined using stellar instantaneous circularities $\lambda_z \equiv L_z/J_{\rm c}$, where L_z is a stellar particle's angular momentum component in the direction of the galaxy's shortest principal axis z found for the stellar component; and $J_{\rm c}$ is the maximum L_z (corresponding to the circular orbit) among all stars that have the same binding energy as the given stellar particle. The three fractions are denoted as $f_{\rm cold}$, $f_{\rm hot}$, and $f_{\rm ccd}$, respectively, all evaluated within a 3D radius of $2R_{\rm hsm}$ from the galaxy center, defined according to the following criteria (for more details, see Xu et al. 2019):

(a) cold component: $\lambda_z > 0.8$;
(b) hot component: $-0.25 < \lambda_z < 0.25$;
(c) counter-rotating cold component: $\lambda_z < -0.6$[2].

We note that all light-related properties are measured in the rest-frame SDSS r-band (Stoughton et al. 2002). All quoted projection-dependent properties are the mean values of the properties measured from three principal projections (along the x, y and z axes) of the simulation box. A simple semi-analytical dust-attenuation model which takes dust extinction and scatter into account, as adopted by Xu et al. (2017), is implemented for the calculations in this work. We also note that the public online catalogue already contains many properties which have similar but subtly different definitions. We specifically use the above-defined properties for this study, having cross-checked our results also against the properties in the public catalogue.

2.2 Galaxy sample selection

The dynamically hot stellar component of a galaxy can in principle build up throughout history and across all galaxy mass scales, provided gravitational instabilities emerge that cause angular momentum loss. This is how, in a nutshell, the spheroidal/bulge components of galaxies and elliptical galaxies in general form. In this study, we aim at understanding "what" the key processes are and "how" they *start* effectively heating up galaxies while they are still actively star-forming and retain disk-dominant morphologies. We focus on systems below a certain galaxy mass scale, such that further complications due to AGN feedback, which can significantly affect star-formation cycles, can largely be avoided (e.g. Dekel & Birnboim 2008). Below, we present the detailed selection criteria adopted for galaxy samples in this study.

To start with, we select all central galaxies (excluding all satellite galaxies) which have stellar masses $M_* \geqslant 5\times10^9\,{\rm M}_\odot$ (below which galaxies may not have enough particles and not be sufficiently resolved), where M_* is the total stellar mass calculated within a radius of 30 kpc from the galaxy center (in order to exclude diffuse stellar components, e.g. Schaye et al. 2015; Pillepich et al. 2018). We employ a combination of two criteria to classify star-forming and disk-dominant galaxies (late-type galaxies), as well as their spheroidal-shaped counterparts with ceased star-formation (early-type galaxies):

(i) Similar to the practice of Genel et al. (2018) and Lu et al. (2020), we classify galaxies by quantifying their distance from the ridge of star-forming main-sequence galaxies. The ridge of main-sequence galaxies is defined as the mean sSFR of galaxies with $M_* < 10^{10.5}\,{\rm M}_\odot$, which yields $\langle \log {\rm sSFR/Gyr^{-1}} \rangle \approx -1.0$ at $z = 0$. Galaxies are classified to be (1) star-forming (late-type galaxies) if their sSFR is larger than 0.5 dex below the ridge, i.e. $\log {\rm sSFR/Gyr^{-1}} \geqslant -1.5$ and (2) quenched (early-type galaxies) if their sSFR is less than 1 dex below the ridge, i.e. $\log {\rm sSFR/Gyr^{-1}} \leqslant -2$.

(ii) A late-type galaxy is also required to have $L_{\rm dev}/L_{\rm tot} < 0.5$[3], i.e. a larger luminosity fraction of disk than bulge. An early-type galaxy is required to meet the opposite criterion.

The two criteria above are applied to all central galaxies at $z = 0$ and within the specified stellar mass range. Galaxies that meet both criteria are classified either into late-types or early-types, making up $\sim 72\%$ of the total central sample at $z = 0$. We confirm that the $g-r$ colour and Sérsic index of the two types of galaxies are naturally well-separated using the criteria above (which can also be seen in Xu et al. 2019, where similar criteria were adopted): most late-type galaxies have $g-r$ colour below 0.65 ($\sim 98\%$) and Sérsic index below 2.5 ($\sim 88\%$), while most early-type galaxies have $g-r$ colour over 0.65 ($\sim 94\%$) and Sérsic index over 2.5 ($\sim 82\%$). We show, in Fig. 1 (left panel), the distribution of all central galaxies in TNG at $z = 0$ on the log sSFR – log M_* plane, colour-coded with

[2] We note that if -0.8 is adopted instead of -0.6 as the criteria for the sake of symmetry, a significant fraction of counter-rotating galaxy sample (see Section 2.2) will be gone, as galaxies simply do not show such extremely negative circularities in any significant fractions of their stellar populations.

[3] We note that in observations, galaxies with pseudo bulges are better described by a Sérsic (rather than a de Vaucouleurs) and an exponential profile and the median value of B/T for S0 galaxies is about 0.38. But in this work, we only use this rough criterion to select galaxies with thin (disk) morphologies.

Table 1. Number of galaxies in different samples. Col.(1): all $z = 0$ central galaxies from the IllustrisTNG Simulation; also the parent sample of Col.(2)−(5). Col.(2): late-type galaxies; Col.(3): selected hot disk galaxies (HDs); Col.(4): selected counter-rotating disk galaxies (CRs); and Col.(5): control-sample normal disk galaxies (NDs). See Section 2.2 for definition and selection criteria.

$N_{\rm central}$	$N_{\rm late-type}$	$N^{\rm sel}_{\rm HD}$	$N^{\rm sel}_{\rm CR}$	$N^{\rm sel}_{\rm ND}$
5681	3177	118	47	165

their bulge luminosity fractions $L_{\rm dev}/L_{\rm tot}$. As can be seen, galaxies with low mass and high sSFR tend to have lower bulge fractions, as theoretically expected.

Among the identified late-type galaxies, we further identify hot disk (HDs) and counter-rotating (CR) galaxies, both of which, as can be seen in later sections, are shown to be dynamically hot. HDs are those where $f_{\rm hot}$ is higher than the mean $f_{\rm hot}$ of the **early-type** sample, which is ~ 0.31 at $z = 0$. CRs are those whose $f_{\rm ccd}$ is larger than 0.2. For comparison, we also define (dynamically cold) normal disk galaxies (NDs) whose $f_{\rm cold}$ is larger than 0.4, above which no HDs and CRs are observed. In addition, we also adopt a further stellar mass cut at $M_* = 2\times10^{10}\,{\rm M}_\odot$ as the upper limit of the three selected samples, in order to eliminate the strong perturbing effects of central AGN activities in these galaxies (e.g. Nelson et al. 2018, fig. 7).

The former two galaxy types (i.e. HDs and CRs) are in fact minorities in the late-type population, while the latter (i.e. NDs) is the majority. We include all HDs and CRs in our dynamically hot galaxy sample, but only randomly select NDs to achieve a sample size equal to the sum of the number of HDs and CRs. This results in 118 HDs, 47 CRs and 165 NDs (see Table 1). We show the distribution of the three samples in the log sSFR − log M_* plane in the right panel of Fig. 1, which is a zoom-in figure with galaxies with $\log M_*/{\rm M}_\odot \in [9.6, 10.3]$ and $\log {\rm sSFR/Gyr^{-1}} \in [-1.5, 0]$. As can be seen, all three sub-populations have roughly similar sSFR, with CRs being slightly lower than the other two. In addition, we have also checked and confirmed that the total halo masses of the three galaxy samples are roughly within the same range.

In Fig. 2, we show the distributions of the three orbital fractions ($f_{\rm cold}$, $f_{\rm hot}$, and $f_{\rm ccd}$) for general late-type galaxies and the three selected samples (HDs, CRs and NDs). As can be seen, the three samples exhibit distinctive differences in cold, hot and counter-rotating cold orbital fractions: NDs, which host the highest fractions in $f_{\rm cold}$, also possess the lowest fractions in $f_{\rm hot}$ and $f_{\rm ccd}$, while HDs indeed have lower fractions in $f_{\rm cold}$ and $f_{\rm ccd}$, and CRs have the lowest fractions in $f_{\rm cold}$ and moderate fractions in $f_{\rm hot}$. This also demonstrates that the three types of galaxies are intrinsically different from each other.

3 WHAT DO THEY LOOK LIKE?

3.1 Morphology of stars and gas

To discuss the visually apparent differences in morphologies between HDs, CRs, and NDs, we first present in Fig. 3 the stellar and HI mass density maps from both edge-on and face-on views for typical HDs (the first 2 columns), CRs (the middle 2 columns), and NDs (the latter 2 columns). As can be seen, the two NDs have the flattest stellar and gaseous disk morphologies with their spin axes well-aligned. In comparison, however, both CRs have less flat stellar and gaseous disks, the spins of which exhibit very large misalignment ($\sim 180°$); the two HDs possess much thicker stellar disks and display the least established gaseous disks among all three types. Interestingly, very often the optical images of NDs and CRs show clear extended spiral patterns which are absent in the HD samples.

In Fig. 4 we show the distributions of several morphology-related key parameters for the stellar components, namely the half stellar mass radius, $\log R_{\rm hsm}$, the surface stellar mass density within $R_{\rm hsm}$, $\log \Sigma_{*,R_{\rm hsm}}$, the shortest-to-longest principal axes ratio of the stellar component, $(c/a)_*$, and the luminosity fraction of the de Vaucouleurs component, $L_{\rm dev}/L_{\rm tot}$. As can be seen, on average NDs appear to be larger and more disky (smaller $(c/a)_*$ and $L_{\rm dev}/L_{\rm tot}$) with lower surface stellar mass densities, while HDs and CRs are smaller and relatively speaking more bulge-dominated (although still having $L_{\rm dev}/L_{\rm tot} < 0.5$) with higher surface stellar mass densities. Specifically, the average sample of CRs has the smallest sizes (as a result, the highest surface stellar mass densities) and the average sample of HDs has the largest $(c/a)_*$ and $L_{\rm dev}/L_{\rm tot}$ among all three galaxy types.

Fig. 5 presents the distributions of three morphological parameters for the gaseous components, namely the shortest-to-longest principal axes ratio $(c/a)_{\rm gas}$, a concentration parameter of HI gas defined as $\gamma_{\rm HI} \equiv m_{{\rm HI},R_{\rm hsm}}/m_{{\rm HI},2R_{\rm hsm}}$, and the HI mass fraction $f_{{\rm HI},2R_{\rm hsm}}$ calculated within $2R_{\rm hsm}$. On average, NDs contain the highest gas fractions $f_{{\rm HI},2R_{\rm hsm}}$ confined within the thinnest disks (lowest $(c/a)_{\rm gas}$) among all three populations. The gas content of HDs and CRs makes up smaller mass fractions and is distributed within thicker disks in comparison. Interestingly, the latter two cases have higher $\gamma_{\rm HI}$ than the former, suggesting that the HI gas in the dynamically hot disk galaxies (especially in HDs), although being of low fraction, is more concentrated in the central regions than in their normal disk counterparts, consistent with the examples showcased in Fig. 3. This is a natural consequence of lower (higher) gas angular momenta in HDs and CRs (NDs), as shall be seen in Section 3.2. Besides, the surface HI mass density in IllustrisTNG is roughly consistent with the result shown in Wang et al. (2016).

3.2 Kinematics of stars and gas

Fig. 6 presents the line-of-sight velocity maps from the edge-on view of both stars and HI gas for our example galaxies. As can be seen, the stellar and HI disks of the two NDs show a co-planar and co-rotating pattern, which is absent in HDs and CRs. The two HDs show much weaker rotation in both stellar and gaseous disks. As shall be seen in Fig. 7, very often HDs exhibit kinematically and morphologically misaligned stellar and gaseous disks. The CR galaxy samples are selected according to hosting a good fraction of counter-rotating stellar orbits, which is indeed revealed by the stellar kinematic maps of the two example CR galaxies. Interestingly, the HI gas therein is in fact also rotating in the opposite direction relative to the bulk stellar population (as indicated by their markedly different spin directions labelled in the figure). In the following sections, we shall see that this is a natural outcome of their evolution.

The misalignment between the (bulk) stellar and the gas components is shown even more clearly in Fig. 7, where we present the distributions of the misalignment angles between **(1)** the spin axes of stellar and gaseous components within $2R_{\rm hsm}$, $\phi_{\rm Gas-STR}$, **(2)** the stellar component and stars formed in the recent 1 Gyr within $2R_{\rm hsm}$, $\phi_{\rm STR-STR(1Gyr)}$, and **(3)** the shortest principal axis and the spin axis of the stellar component, $\phi_{*,\rm MOR-KIN}$ (from left to right). As shown in the figure, while NDs always have well aligned stellar and gaseous disks, HDs and CRs exhibit remarkably large misalign-

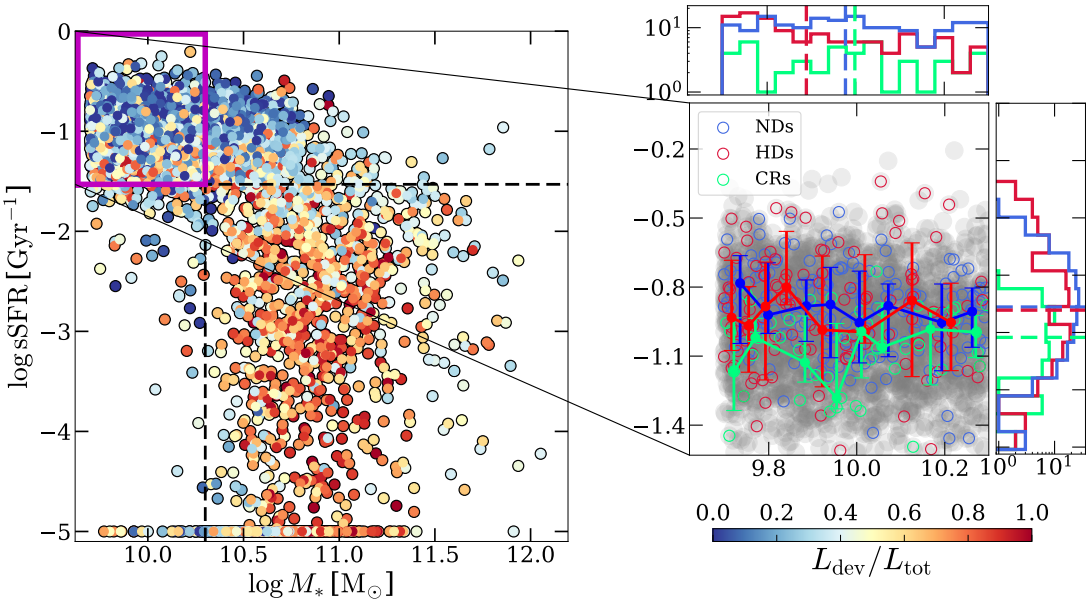

Figure 1. Left: specific star-formation rate log sSFR versus stellar mass log M_* for all central galaxies in TNG at $z = 0$, colour-coded with the bulge component luminosity fraction $L_{\rm dev}/L_{\rm tot}$. The black dashed lines indicate $M_* = 2 \times 10^{10}\,{\rm M}_\odot$ and log sSFR/Gyr$^{-1} = -1.5$, respectively. Right: zoom-in distribution of galaxies with log $M_*/{\rm M}_\odot \in [9.6, 10.3]$ and log sSFR/Gyr$^{-1} \in [-1.5, 0]$, in which all the galaxies in this region are indicated by grey circles and normal disks (NDs), hot disks (HDs), and counter-rotators (CRs) are indicated with blue, red, and green circles, respectively. The median profile of the three samples are indicated with blue, red, and green lines with error bars indicating the range from the 16th to the 84th percentiles (1σ).

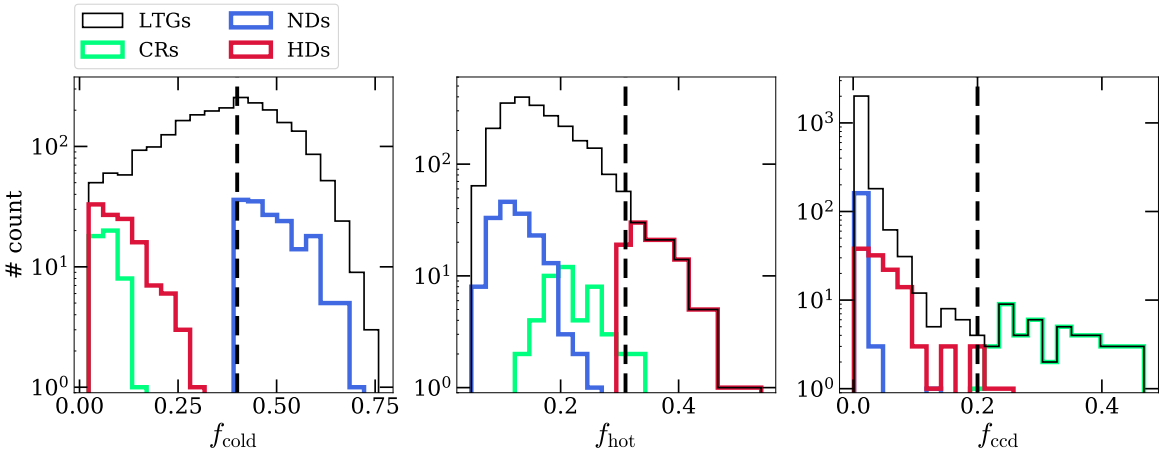

Figure 2. Distributions of $f_{\rm cold}$, $f_{\rm hot}$ and $f_{\rm ccd}$ (from left to right, see Section 2.1 for definitions) for late-type galaxies (black), NDs (blue), HDs (red), and CRs (green). Black dashed lines represent $f_{\rm cold} = 0.4$, $f_{\rm hot} = 0.31$, and $f_{\rm ccd} = 0.2$, which are used to classify NDs, HDs, and CRs, respectively.

ment: the angles $\phi_{\rm Gas-STR}$ and $\phi_{\rm STR-STR(1Gyr)}$ for most of the HDs occupy the range between $\sim 0^\circ - 90^\circ$; while the CRs show these two misalignment angles typically between $\sim 90^\circ - 180^\circ$, revealing their gaseous disks rather than tracing the youngest stellar populations, both of which are counter-rotating with respect to the spin of the bulk (older) stellar populations. Besides, HDs and CRs expand their $\phi_{*,\rm MOR-KIN}$ up to $\sim 50^\circ$, while NDs rarely have $\phi_{*,\rm MOR-KIN}$ over 10°. In Fig. 8 we show the distributions of the stellar and gaseous spins for the three galaxy samples. In general, NDs possess the highest spins while HDs and CRs have weaker co-rotation, as is also demonstrated in Fig. 6 for example galaxies.

Observationally, the stellar spin of a galaxy is difficult to measure directly. A good observational indicator is V_*/σ_*, where V_* is the line-of-sight velocity and σ_* is the dispersion, both of which can be obtained directly from spectroscopic observations. In Fig. 9 we show the average radial profile of V_*/σ_* for the three galaxy samples. Here the V_*/σ_* profile of each galaxy is calculated in a long slit along the semi-major axis from the galaxy's edge-on view, with a width of $0.5R_{\rm hsm}$. As can be seen in the left panel, while NDs show steeply increasing V_*/σ_* profiles towards larger radii with $V_*/\sigma_* \sim 3.5$ at $r = 2R_{\rm hsm}$, HDs and CRs both show flatter V_*/σ_* profiles with $V_*/\sigma_* \sim 2$ and ~ 1.3 at $r = 2R_{\rm hsm}$, respectively, again indicating their weaker co-rotation in comparison. On the right, the V_*/σ_* profiles of young stars (formed in the recent 1 Gyr) are pre-

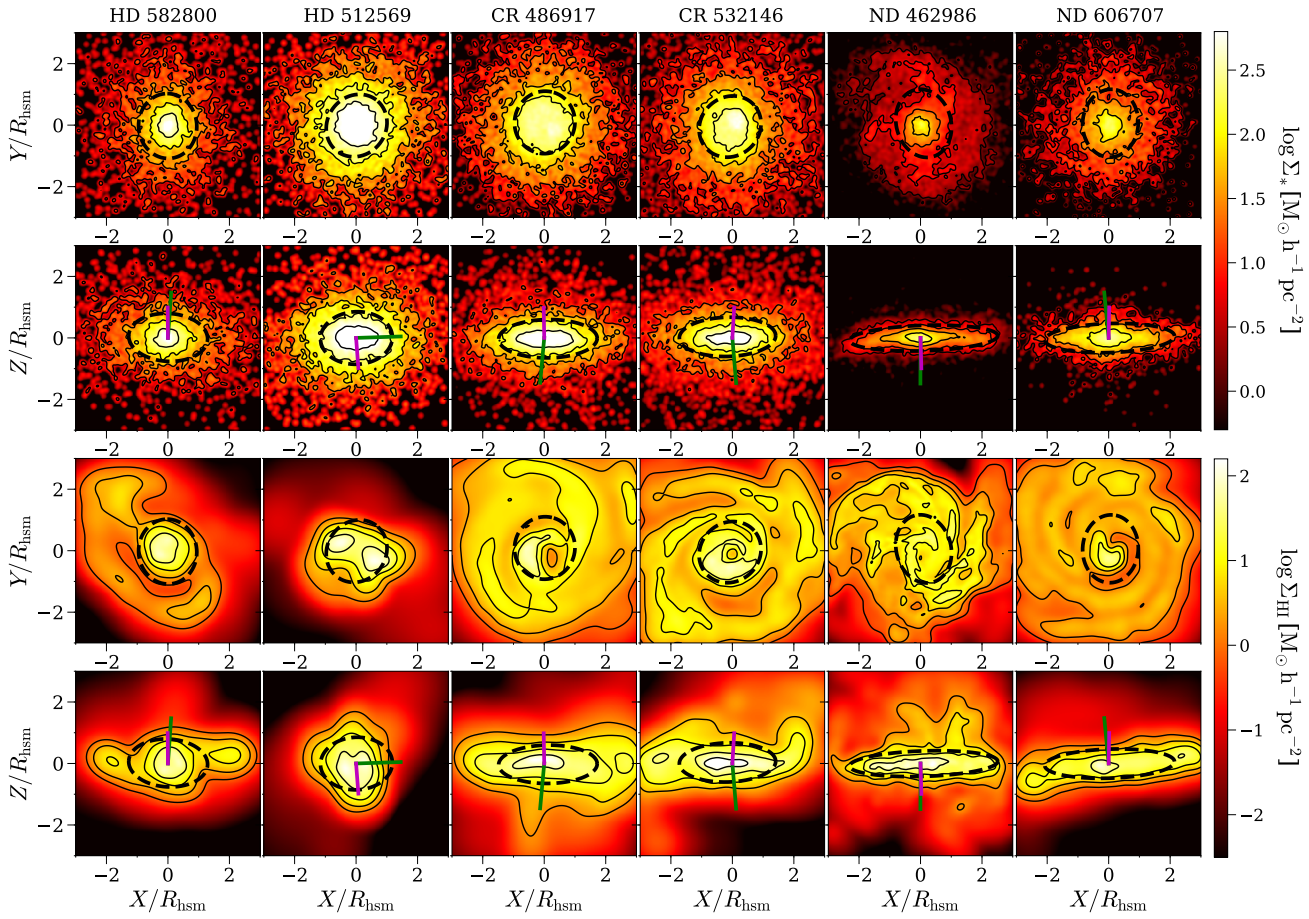

Figure 3. Examples of two HDs (ID: 582800, 512569), two CRs (ID: 486917, 532146), and two NDs (ID: 462986, 606707) from left to right. For each example, we show from the top to the bottom rows: **(1)** the face-on view of the stellar mass density map, **(2)** the edge-on view of the stellar mass density map, **(3)** the face-on view of the HI gas surface mass density map, and **(4)** the edge-on view of the HI gas surface mass density map. The black dashed ellipses indicate the position angle and the ellipticity of the *stellar* component for face-on (Row 1) and edge-on (Row 2) views, respectively. Contours of the surface mass densities are shown every 0.5 dex with a set of black curves. In the edge-on maps, the purple and green lines indicate the spin axes of stellar and gaseous components, respectively.

sented. For HDs, the V_*/σ_* profile remains flatter with a ratio ~ 1.2 at $r = R_{\rm hsm}$. Note that strong rotation features as indicated by large V_*/σ_* are clearly seen both for NDs and CRs, with a ratio of ~ 4 at $r = R_{\rm hsm}$.

The above described behaviour of V_*/σ_* among the three galaxy samples can be better understood and demonstrated from the perspective of stellar orbits. In Fig. 10, we present the distribution of circularity λ_z ($\equiv L_z/J_{\rm c}$, see definition in Section 2.1) for our example galaxies. As shown in the figure, the total (black solid) circularity distributions of NDs show clear peaks towards $\lambda_z \sim 1$, while CRs also exhibit an increasing tail towards $\lambda_z \sim -1$, indicating the existence of a good fraction of counter-rotating stellar population. Unlike the two types above, HDs host a significant fraction of low-angular momentum ($\lambda_z \sim 0$) orbits. When considering only stars that formed over 8 Gyrs ago, their circularity distributions (red) can be dominated by either a low-angular momentum component (with λ_z peaking close to zero) or high-angular momentum circular orbits already existing by then. Stars that formed less than 1 Gyrs ago may exhibit different orbital distributions (blue) from those who have formed earlier-on. Newly-formed stars in NDs have circularities significantly peaking at $\lambda_z \sim 1$, indicating a strongly established co-rotating disk at the current epoch, while those in CRs clearly occupy counter-rotating orbits ($\lambda_z \sim -1$). Newly-formed stars in some of the HDs behave quite similarly to those in CRs (e.g., HD 512569). Such HDs in fact used to be CRs at earlier times (see next section for more details). There are also HDs which have always been dominated by hot orbits ($\lambda_z \sim 0$, e.g., HD 582800) throughout their histories.

It is worth noting that when we combine all above-mentioned kinematic properties of gas and stars, we find that in CR galaxies, newly formed stars in fact follow circular motions, as a consequence of being formed in gaseous disks that are counter rotating with respect to the bulk (older) stellar populations in these systems. This was also reported in Starkenburg et al. (2019), who studied possible formation scenarios of low-mass counter-rotating galaxies in the Illustris simulation (Vogelsberger et al. 2013, 2014a,b; Genel et al. 2014; Nelson et al. 2015). In Section 4, we present some alternative origins added to their formation picture.

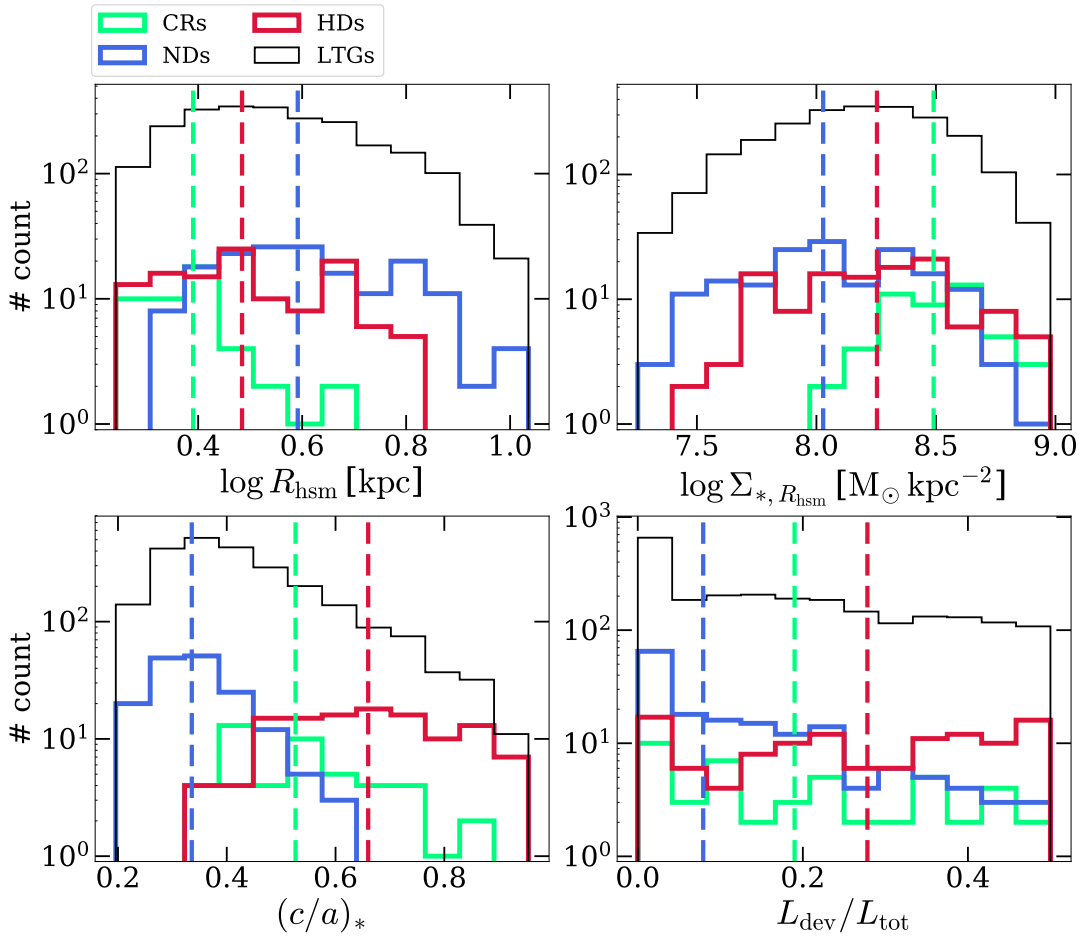

Figure 4. Distributions of galaxy size, log $R_{\rm hsm}$ (upper left), surface mass density within $R_{\rm hsm}$, log $\Sigma_{*,R_{\rm hsm}}$ (upper right), the shortest-to-longest principal axes ratio of stellar component, $(c/a)_*$ (bottom left), and de Vaucouleurs to total luminosity ratio, $L_{\rm dev}/L_{\rm tot}$ (bottom right). In each panel, the dashed lines indicate the median values of the corresponding property of NDs (blue), HDs (red), and CRs (green).

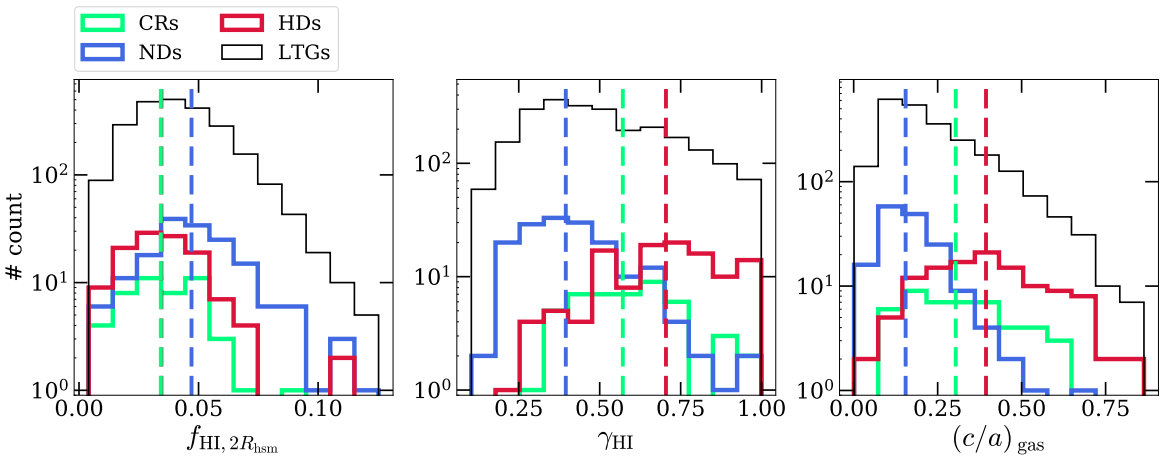

Figure 5. Distributions of HI mass fraction within $2R_{\rm hsm}$, $f_{\rm HI,2R_{\rm hsm}}$ (left), the ratio of HI mass within $R_{\rm hsm}$ and $2R_{\rm hsm}$, $\gamma_{\rm HI}$ ($\equiv M_{\rm HI,R_{\rm hsm}}/M_{\rm HI,2R_{\rm hsm}}$, middle), and the shortest-to-longest principal axes ratio of gas, $(c/a)_{\rm gas}$ (right). The symbols are the same as in Fig. 4.

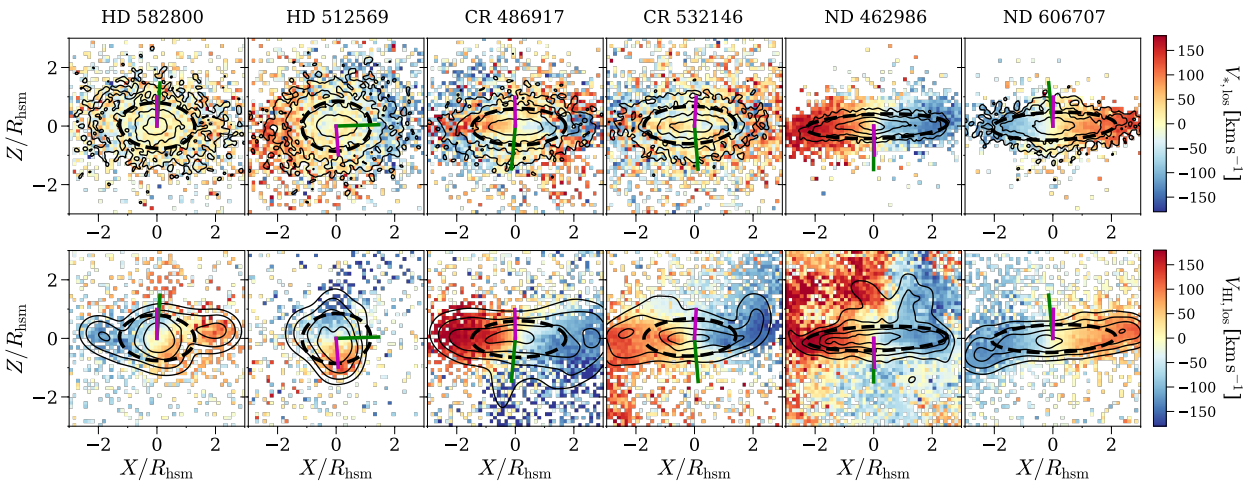

Figure 6. Examples of two HDs (ID: 582800, 512569), two CRs (ID: 486917, 532146), and two NDs (ID: 462986, 606707) from left to right. For each example, we show **(1)** the edge-on view of the line-of-sight velocity map of the stellar component (top row) and **(2)** the edge-on view of the line-of-sight velocity map of HI gas (bottom row). In each panel, the position angle and the ellipticity of the *stellar* component from edge-on view are indicated by the black ellipse, with purple and green lines indicating the spin axes of the stellar and gaseous components, respectively; contours of surface mass density are shown every 0.5 dex by a set of black curves.

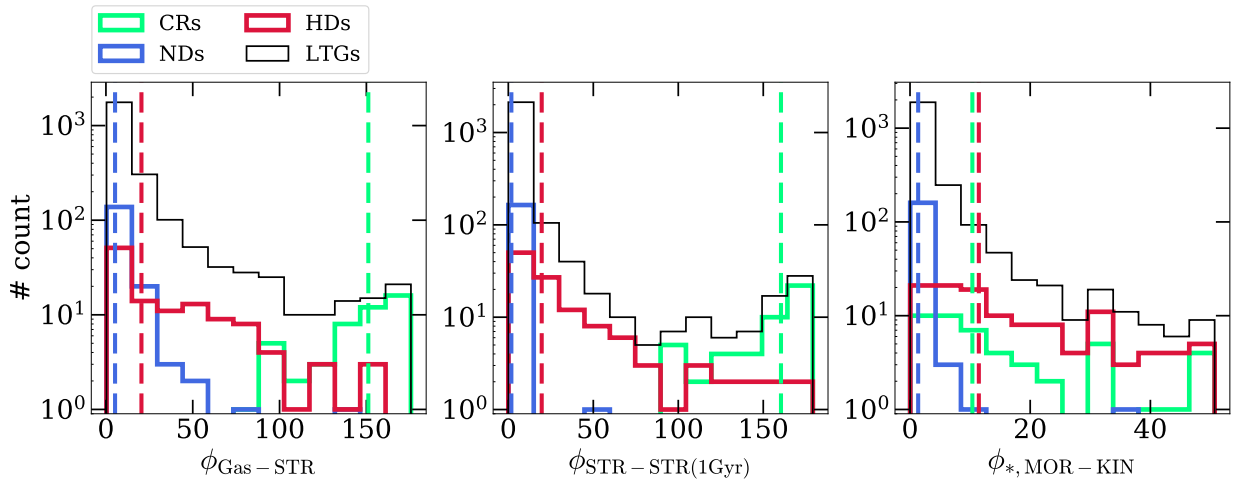

Figure 7. Distributions of misalignment angles between **(1)** the kinematic major axes of gas and stars, $\phi_{\rm Gas-STR}$, **(2)** the kinematic major axes of stars, and young stars formed in the recent 1 Gyr, $\phi_{\rm STR-STR(1Gyr)}$, and **(3)** the photometric and kinematic major axes of stars, $\phi_{*,\rm MOR-KIN}$ from left to right. The symbols are the same as in Fig. 4.

3.3 Star-formation activities

In this section, we show the comparison of star-formation activities among the three galaxy samples. We first present the star-formation-rate maps for the six example galaxies in Fig. 11. As can be seen, the two NDs typically have extended star-formation activities (out to $\sim 3R_{\rm hsm}$), while star-formation in the two HDs is strongly constrained within the central regions; the two CRs exhibit both a core and fairly extended star-forming distributions. We attribute this central concentration in star-formation in these dynamically hot systems to the lower gas angular momenta therein (see Fig. 8).

To better illustrate the differences in the spatial distributions of star-formation activities among the three galaxy samples, we show in Fig. 12 the specific star-formation-rate (sSFR) and stellar age profiles as a function of radius out to $2R_{\rm hsm}$ from the galaxy center. As can be seen, HDs (red) have on average the most concentrated star formation, which is also the strongest among the three galaxy samples, as far as the central regions are concerned. As a consequence, the central stellar populations therein are significantly younger than the outskirts as well as those in the ND and CR counterparts. In contrast, NDs (blue) have fairly flat/extended[4] distributions in both sSFR and stellar age. In comparison, NDs have the highest sSFR and the youngest stellar ages at larger disk radii among all three

[4] We note that the ND samples in this study are selected to be of lower-masses and have not established their bulge components therefore the age distributions in these systems do not yet show a significantly older population in the central regions as expected from the "inside-out" growth model.

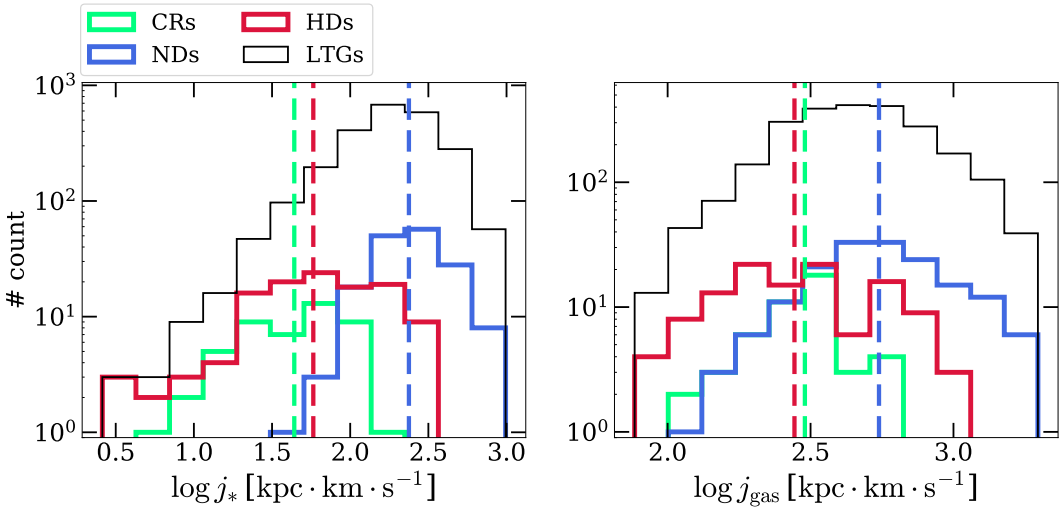

Figure 8. Distributions of spin of the stellar component log j_* (left) and the gas component log $j_{\rm gas}$ (right). The symbols are the same as in Fig. 4.

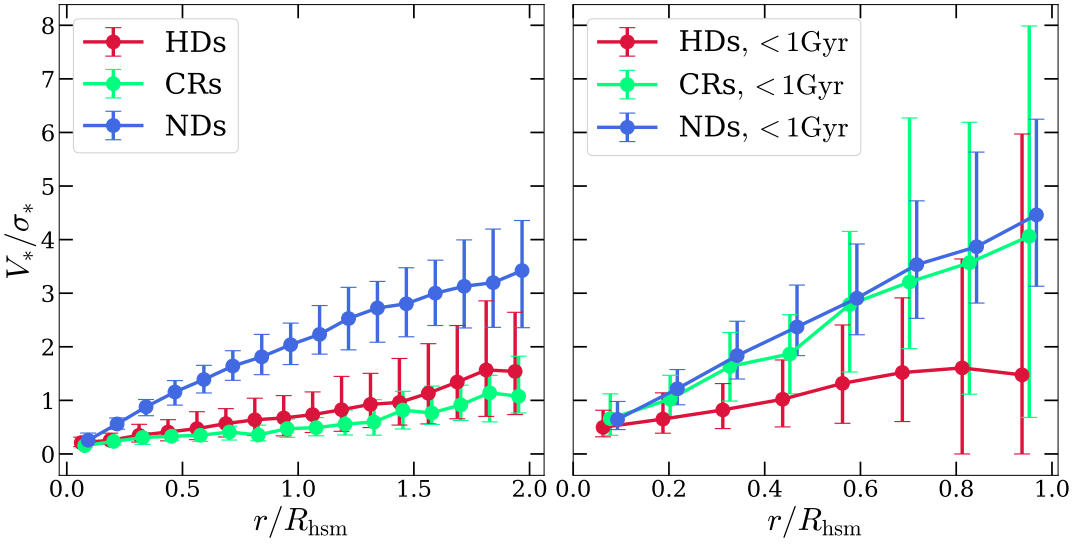

Figure 9. Radial V_*/σ_* profiles for HDs (red), CRs (green), and NDs (blue), where V_* is the line-of-sight velocity and σ_* is the dispersion. For each galaxy, both V_* and σ_* are calculated in a slit with its width being $0.5R_{\rm hsm}$ along the major axis from the edge-on view of the galaxy. The left panel shows the V_*/σ_* profiles of all stars in the slit and the right panel shows the V_*/σ_* profiles of stars formed in the recent 1 Gyr (shared y-axis with the left panel). The error bars indicate the range from the 16th to the 84th percentiles (1σ).

galaxy samples. On the other hand, CR galaxies (green) bear some resemblances to both HDs and NDs: centrally-concentrated star-formation is clearly seen, while at larger radii, sSFR therein does not as quickly drop as in HDs, but is not yet as high as in NDs. We discuss the reasons for these behaviours in Section 4.

4 HOW DO THEY FORM?

Starkenburg et al. (2019) investigated the origin of gas-star counter-rotating (star-forming) systems using the Illustris simulation, and found that the formation is firstly associated with a major episode of gas removal through two effective channels, namely AGN feedback and fly-by passages (identified as being satellite galaxies prior to counter-rotating), followed by new gas accretion in anti-aligned directions. In this study, in order to understand the origin of all three selected galaxy samples in the IllustrisTNG simulation, we make use of the SUBLINK tree (Rodriguez-Gomez et al. 2015) provided by the IllustrisTNG team to trace the entire evolution of the simulated galaxies up to $z = 2$. This allows us to examine the connections between their evolutionary origin, their star-forming and AGN feedback activities, their gas content variations, their stellar and gas spin evolution, as well as their galaxy merger histories. We find that this last aspect plays a crucial role in shaping the morphological and kinematic evolution of the galaxies examined in this study.

Apart from the properties of the investigated galaxies along their main evolutionary branches, we also employ three quantities to characterize the mergers the galaxies experienced: merger orbit angle $\theta_{\rm orb}$, merger mass ratio μ, and merger gas fraction $f_{\rm g}$. Here

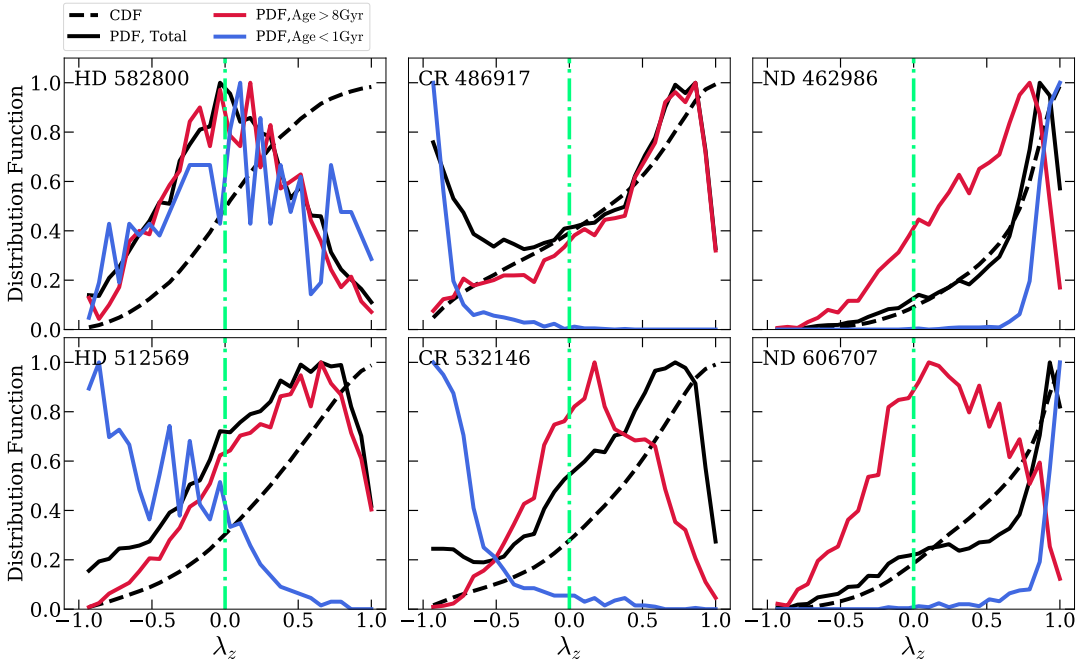

Figure 10. The distribution of circularity λ_z ($\equiv L_z/J_c$) of two example HDs (ID: 582800, 512569), two example CRs (ID: 486917, 532146), and two example NDs (ID: 462986, 606707) from left to right. In each panel, the black dashed curve represents the CDF of L_z/J_c and the black solid curve shows the PDF of all stars within $2R_{\rm hsm}$; the PDFs of stars formed 8 Gyr ago and within the recent 1 Gyr (both are within $2R_{\rm hsm}$) are shown by red and blue curves, respectively. The green dotted-dashed line indicates $\lambda_z = 0$.

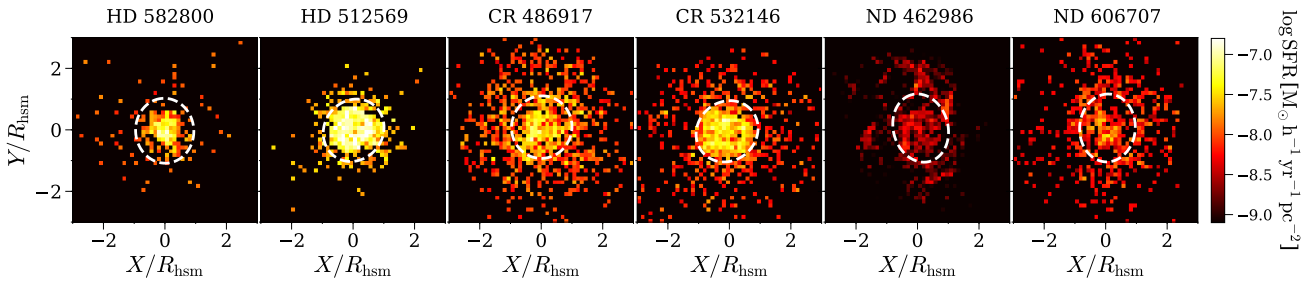

Figure 11. Examples of two HDs (ID: 582800, 512569), two CRs (ID: 486917, 532146), and two NDs (ID: 462986, 606707) from left to right. For each example, we show the face-on map of its star-formation rate density in the recent 1 Gyr, with the white ellipse indicating the position angle and ellipticity obtained from the face-on view of the example.

$\theta_{\rm orb}$ is defined as the angle between the orbital angular momentum of the in-coming galaxy (measured at the time when the galaxy has the highest stellar mass across its evolution history) and the spin of the host galaxy at that snapshot. Thus, $\theta_{\rm orb} > 90^\circ$ means that the orbital spin of the in-coming galaxy is counter-rotating with respect to the spin of the host galaxy. The merger mass ratio μ is defined as

$$\mu = \frac{M_{*,\rm incoming}}{M_{*,\rm host}}, \quad (1)$$

where $M_{*,\rm incoming}$ and $M_{*,\rm host}$ are the stellar masses of the in-coming galaxy and the host galaxy within $2R_{\rm hsm}$, respectively. The merger gas fraction is defined as

$$f_{\rm g} = \frac{M_{\rm gas,incoming} + M_{\rm gas,host}}{M_{\rm total,incoming} + M_{\rm total,host}}, \quad (2)$$

where $M_{\rm gas,incoming}$ and $M_{\rm gas,host}$ are gas masses of the in-coming galaxy and the host galaxy, while $M_{\rm total,incoming}$ and $M_{\rm total,host}$ are the total masses (including stellar masses and dark matter masses) of the two galaxies, respectively. All these masses are measured within a 3D aperture of radius equal to $2R_{\rm hsm}$.

4.1 Two example ND galaxies

Fig. 13 shows the evolution of two example NDs taken from our sample. As can be seen, the angular momenta of both stellar and gas components grow steadily. The misalignment between the gas and stellar spins decreases, and both the stellar and gas disks become thinner and thinner as the dynamically cold stellar orbits build up. Galaxy ND 462986 has experienced very frequent gas-rich mergers

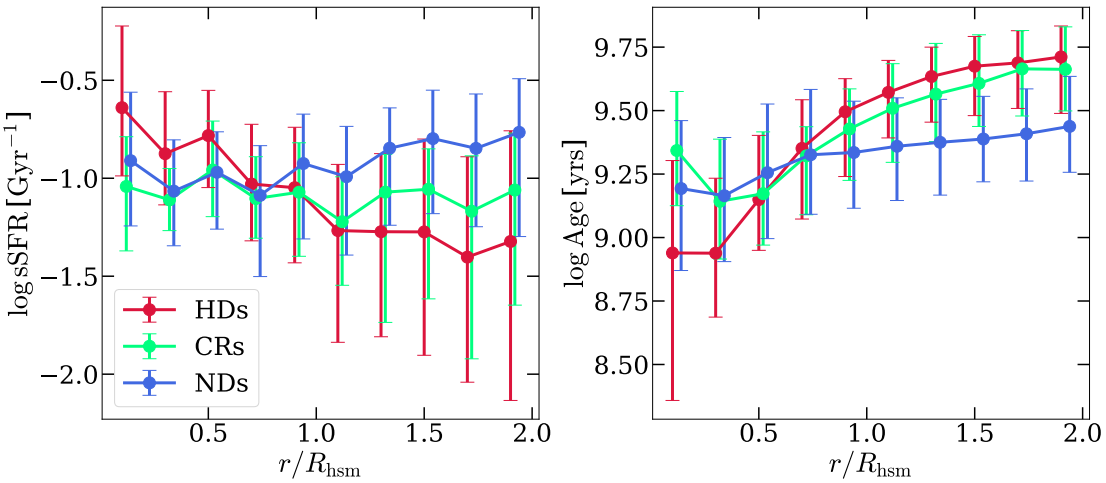

Figure 12. Radial profiles of the specific star-formation rate (log sSFR, left) and age (log Age, right). HDs, CRs, and NDs are represented by red, green, and blue lines, respectively. The error bars indicate the range from the 16th to the 84th percentiles (1σ).

while Galaxy ND 606707 has undergone only one recorded merger, but both have successfully established their disk morphology and rotational kinematics with active star-formation at the current epoch.

4.2 Two example HD galaxies

Figure 14 shows the evolution of two example HDs selected from our sample. Galaxy HD 582800 has always been dynamically hot and never been able to grow its disk properly. This can be seen from the evolution of its hot and cold orbit fractions (4th panel, left), as well as from the circularity distributions in age bins (Fig. 10, upper left panel). It is interesting to note that around $z = 0.5$ this galaxy was a satellite of a bigger system for a while (indicated by the grey shaded regions), during and after which both the stellar and gas disks became thicker, and the cold orbital fraction decreased further while the counter-rotating disk component also started growing. By $z = 0$ this galaxy remains a dynamically hot system.

Galaxy HD 512569 has experienced a different evolutionary history. It started with being a well established disk at $z \sim 1$ with a dominant (low) fraction of cold (hot) stellar orbits and thin morphologies in both stellar and gaseous disks. Two mergers that initiated just before $z = 1$ and finished by $z = 0.7$ have caused a significant decrease of the cold orbit fraction as well as an increase of disk thickness, which carry through its following evolution. Meanwhile, the misalignment between the gas and stellar spins started building up. Shortly after another merger event which started at $z \sim 0.5$ and finished at $z \sim 0.3$ with a retrograde in-coming satellite, the counter-rotating orbit fraction increases (as can also be seen in the age-binned circular distribution in the bottom left panel of Fig. 10), and the misalignment started growing significantly. By the current epoch, this system has lost its rotation-supported thin disk and has become dynamically hot.

The example hot disks show two typical but different evolutionary paths: in the former case, a normal flat and rotation supported disk never succeeded to grow, while in the latter case, a normal disk at high redshift became hot at some point due to a galaxy interaction/merger. In some cases, a normal disk can first go through a phase of CR before eventually becoming a HD. In some other cases, like HD 512569, the outcome that the galaxy has a high fraction of hot orbits essentially arises as a consequence of a significant growth of counter-rotating orbits in its most recent history. We stress that being dynamically hot is mostly a transient state depending on local conditions of galaxy merger/interactions, rather than an age-dependent evolution phase.

It is worth noting that the correlations between the emergence of hot kinematic signatures (morphological – in 3rd panel, and orbital – in 4th panel) and strong AGN feedback activities (as indicated by the high black hole accretion rates; 2nd panel, right) are not evident in most dynamically hot galaxies. For Galaxy HD 582800 and a few other galaxies alike, sudden increases in the black hole accretion rate are always accompanied by merger events. This may indicate that the activity of central black holes and AGN feedback may not have played a leading role in the formation of the dynamically hot disk galaxies at the investigated mass scale.

4.3 Two example CR galaxies

Fig. 15 shows the evolution of two example CR galaxies in this study. Galaxy CR 486917 had has a rotation-supported thin stellar disk for quite some time in its history until just before $z \sim 0.5$, when two successive retrograde mergers happened, shortly after which the SFR shot up temporarily, the cold orbital fraction started decreasing, and misalignment begun to grow significantly. With another delay in time, the counter-rotating orbit fraction started increasing by $z \sim 0.2$, and the system finally became a CR at the current epoch. For Galaxy CR 532146, what terminated the steady growth of its rotation-supported disk was a recorded retrograde merger that happened at $z \sim 0.3$, after which the disk became thicker, and both the gas-star misalignment and the counter-rotating stellar orbits built up.

It is worth noting that correspondences between retrograde merger events (shown by down arrows) and the subsequent build up of counter-rotating orbital fractions are clearly seen in many CR systems. Very often, a decrease in gas spin and an increase first in the outer-gas misalignment angle are observed to go together, prior to and during a large-angle merger event, which is then followed by a (delayed) rise in the inner-gas misalignment angle as well as a rebuild of gas spin (after counter-rotating gas has been substantially accreted to the galaxy center). During this process, the central gas fraction would decrease after the merger event but the change is not

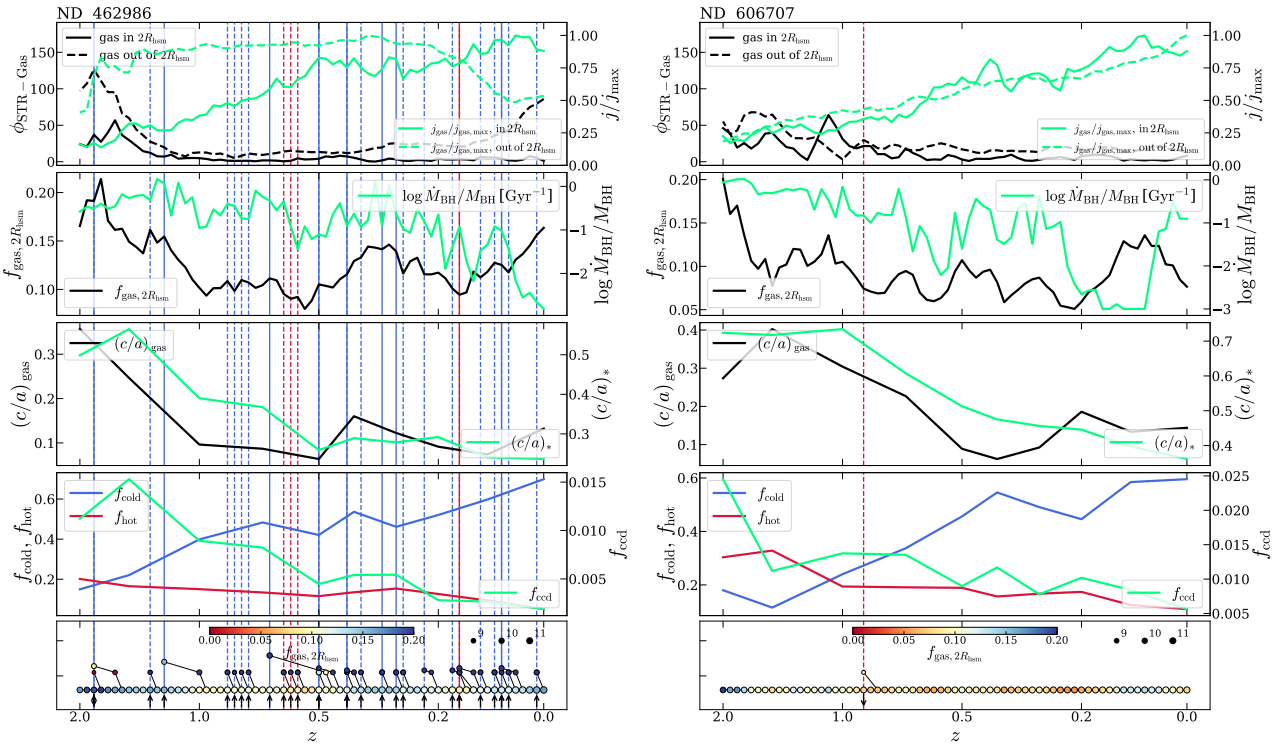

Figure 13. The redshift evolution ($0 \leqslant z \leqslant 2$) of properties for the two ND examples (IDs: 462986, 606707). The properties are **(1)** the spin axes misalignment of gas within (black solid) and out of $2R_{\rm hsm}$ (black dashed) with respect to stars within $2R_{\rm hsm}$, $\phi_{\rm STR-Gas}$ (1st panel, left Y-axis); **(2)** the spin of gas within (green solid) and out of $2R_{\rm hsm}$ (green dashed), $j_{\rm gas}/j_{\rm gas,max}$ (normalized to its maximum in the history, 1st panel, right Y-axis); **(3)** gas fraction within $2R_{\rm hsm}$, $f_{\rm gas,2R_{hsm}}$ (black solid, 2nd panel, left Y-axis); **(4)** black hole accretion rate, $\log \dot{M}_{\rm BH}/M_{\rm BH}$ (green solid, 2nd panel, right Y-axis); **(5)** the shortest-to-longest axis ratio for gas, $(c/a)_{\rm gas}$ (black solid, 3rd panel, left Y-axis); **(6)** the shortest-to-longest axis ratio for the stellar component, $(c/a)_*$ (green solid, 3rd panel, right Y-axis); and **(7)** 3 types of orbital fractions (4th panel): $f_{\rm cold}$ (blue solid, left Y-axis), $f_{\rm hot}$ (red solid, left Y-axis), and $f_{\rm ccd}$ (green solid, right Y-axis). For each example, we show its merger history in the bottom panel, with circle sizes indicating the stellar mass within $2R_{\rm hsm}$ and colours indicating the gas fraction within $2R_{\rm hsm}$ of galaxies at different redshifts. For each merger event, we show both the in-coming galaxy and its progenitor at the snapshot when it reaches its maximum stellar mass. In each panel, each merger event is indicated by a vertical line with its colour encoding the merger being wet ($f_{\rm g} \geqslant 0.1$, blue) or dry ($f_{\rm g} < 0.1$, red) and line style marking the merger mass ratio ($\mu < 0.01$: dashed; $\mu \geqslant 0.01$: solid). In the bottom of the merger tree, the arrows represent the orbital angle of the in-coming galaxy with respect to the spin of the host galaxy, $\theta_{\rm orb}$ ($\theta_{\rm orb} < 90°$: up arrow; $\theta_{\rm orb} \geqslant 90°$: down arrow). See Section 4 for definitions of $f_{\rm g}$, μ, and $\theta_{\rm orb}$.

always sharp. In other words, a clear phase of gas removal, as found by Starkenburg et al. (2019) is not always present in the CR galaxies in our study. It is also worth noting that, in Khoperskov et al. (2021), 25 counter-rotating TNG galaxies of a similar mass range as in this work were studied. They also discovered the connection between the counter-rotation of the stellar component and the external gas infall which captures and mixes with the pre-existing gas, resulting in counter-rotating gaseous disks.

4.4 Merger statistics

From examining individual cases (as demonstrated for the example galaxies above), we realize that mergers may have played an important role in the formation of dynamically hot galaxies and in causing morphological and kinematic differences among the three galaxy types. In order to reveal these connections in a statistical fashion, we further define merger types according to merger orbit angle $\theta_{\rm orb}$, merger mass ratio μ and merger gas fraction $f_{\rm g}$, and carry out merger number counts (per galaxy) since $z = 1$ for the different merger types. We note here that we have also carried out the same analysis on the mergers from $z = 2$ to $z = 0$ and found that the main results are nearly unchanged, except that the discrepancies between the three types of galaxies become smaller. That is because galaxies of the studied mass range may have experienced similar merger histories at higher redshift (i.e. $z > 1$). In addition, the progenitors of the studied galaxies are getting close to the resolution limit at these high redshifts, preventing us from extracting galaxy properties reliably. All analyses hereafter are thus carried out for mergers since $z = 1$. The result is presented in Table 2.

As can be seen, NDs experienced on average the most frequent galaxy mergers among all three galaxy samples, CRs experienced the least, and HDs lie in between. One significant difference among them is the fraction of merger events where the in-coming galaxy merges with an orbit angular momentum opposite to that of the main galaxy spin (i.e., $\theta_{\rm orb} \geqslant 90°$): this fraction is as high as 57% among CRs but only 14% for NDs and 24% for HDs. It is indeed seen in over half of the CR cases, as well as some of the HDs, where gas-star misalignment and growth of counter-rotating orbits emerge shortly after a retrograde merger event (as is seen for CR 486917, CR 532146 and HD 512569). It is then not surprising to find that the coherent rotations of NDs have survived the (albeit more frequent) pro-grade mergers, which make up 86% of averaged merger events for a ND galaxy.

The average numbers of mergers which have mass ratio $\mu \geqslant$

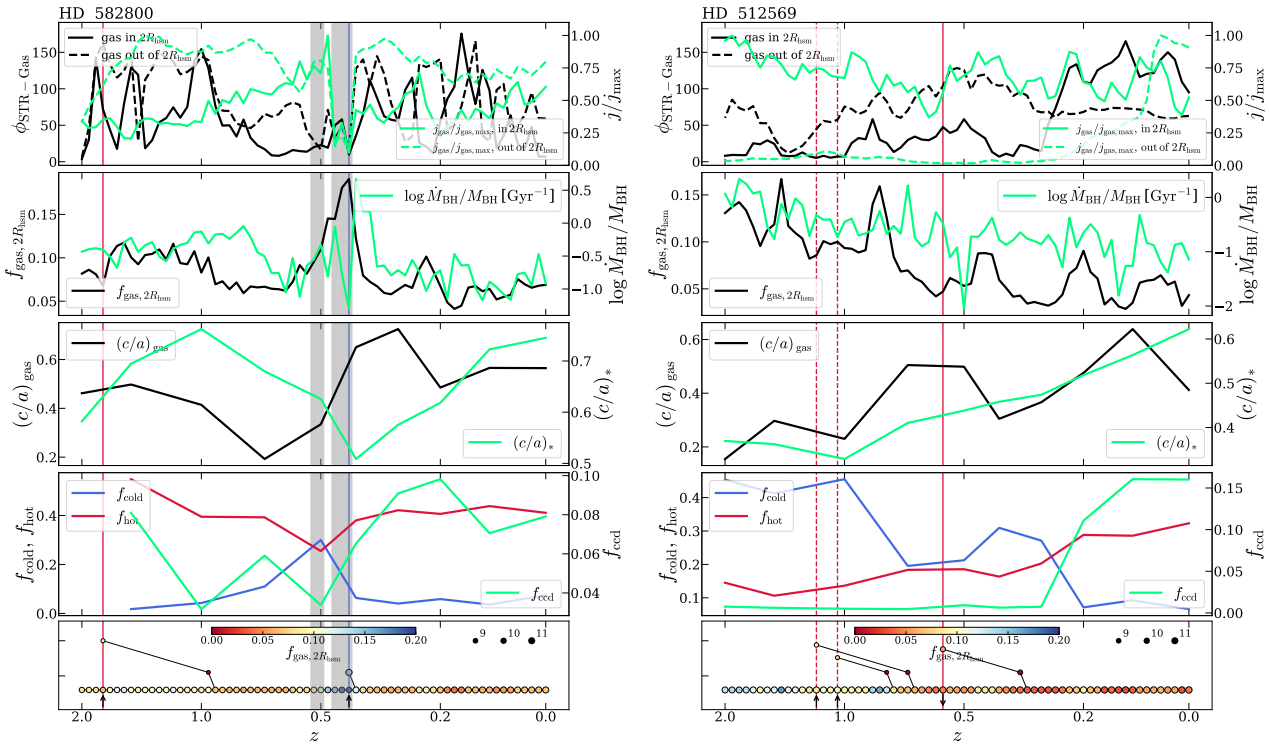

Figure 14. The redshift evolution ($0 \leqslant z \leqslant 2$) of properties for the two HD examples (IDs: 582800, 512569). The symbols are the same as in Fig. 13. The grey shaded regions indicate the period when the host galaxy is not a central galaxy.

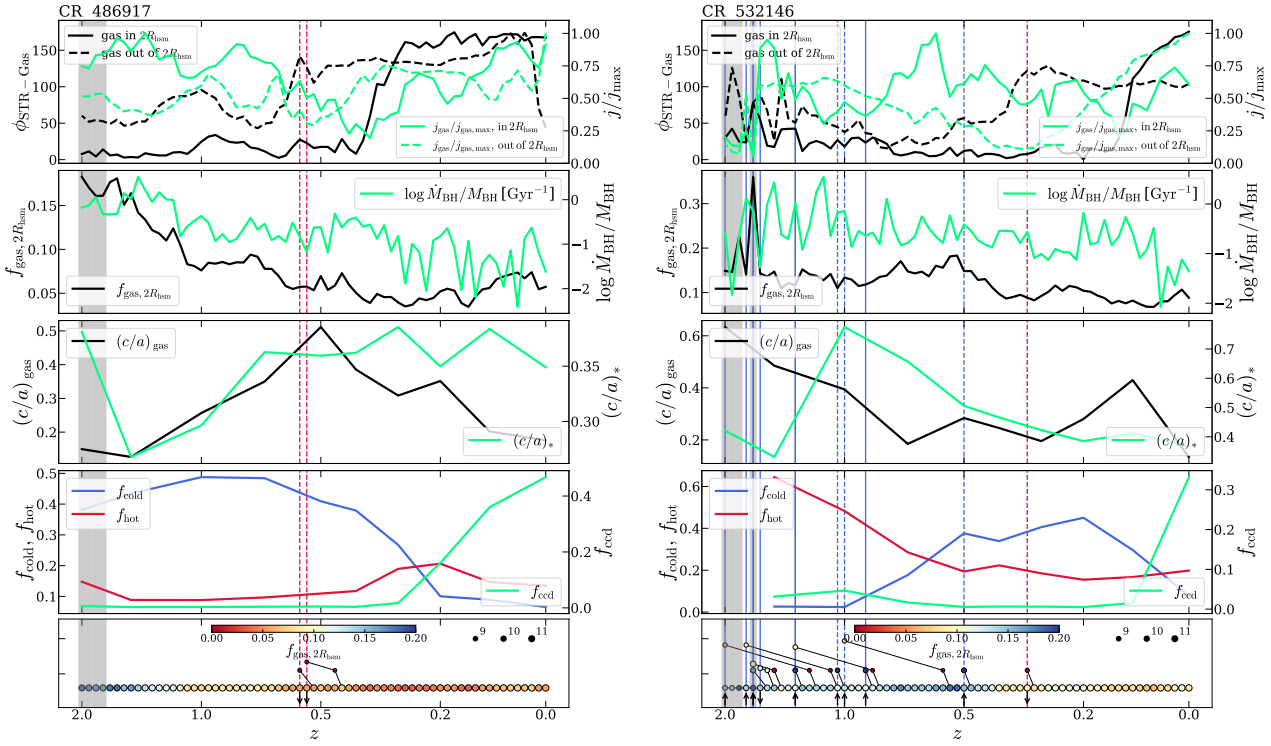

Figure 15. The redshift evolution ($0 \leqslant z \leqslant 2$) of properties for the two CR examples (IDs: 486917, 532146). The symbols are the same as in Fig. 13. The grey shaded regions indicate the period when the host galaxy is not a central galaxy.

0.01 also differ markedly from nearly half (46%) for HDs, 39% for CRs, to 28% for NDs. This might serve as marginal evidence that larger-mass ratio merger events are more likely to induce the hot dynamical configuration of a galaxy, however, on an individual bases this connection is not clearly established.

It is interesting to note that CRs have the largest fractions in gas-rich mergers (i.e., $f_g \geqslant 0.1$), up to 70%, followed by 60% for NDs and 51% for HDs. The supply of new gas brought in due to mergers is however crucial for newer generations of star-formation. In the case of CRs, these gas-rich merger events together with their retrograde merging fashion, may have provided the basis for the counter-rotating newer-generations of stellar populations.

5 REAL-WORLD COUNTERPARTS

In this section, we present a sample of observed late-type galaxies which have misaligned gaseous and stellar spin axes from the MaNGA Product Launch-7 (MPL7), which contains 4621 galaxies and is identical to the MaNGA data included in the SDSS data release 15 (DR15; Aguado et al. 2019). We show that these gas-star misaligned galaxies are very plausible real-world counterparts of our HDs and CRs selected from the IllustrisTNG Simulation according to their stellar orbit features.

To get the type and misalignment angle of MaNGA galaxies, we follow the methods of Jin et al. (2016), where star-forming galaxies are identified according to their locations on the log SFR − log M_* plane and the misalignment angles are defined as $\Delta\mathrm{PA} = \left|\mathrm{PA}_* - \mathrm{PA}_{\mathrm{gas}}\right|$ (where PA_* and $\mathrm{PA}_{\mathrm{gas}}$ are the position angles of stars and gas, measured using the FIT_KINEMATIC_PA routine described in Krajnović et al. 2006). Thus, the misaligned star-forming galaxies are defined to be galaxies with log SFR $> 0.86 \times \log M_* - 9.29$ and $\Delta\mathrm{PA} > 30°$ (see Jin et al. 2016, section 2.2.2 and 2.2.3). The velocity field data used here are extracted from the IFU spectra using the MaNGA data analysis pipeline (DAP; Westfall et al. 2019) by fitting absorption lines, making use of the PPXF software (Cappellari & Emsellem 2004; Cappellari 2017) with a subset of the MILES (Sánchez-Blázquez et al. 2006; Falcón-Barroso et al. 2011) stellar library, MILES-THIN. Before fitting, the spectra are Voronoi binned (Cappellari & Copin 2003) to S/N = 10. Besides, we derive the extended stellar population properties from the MaNGA Pipe3D Value Added Catalog (VAC; Sánchez et al. 2018). Redshift and effective radii of these galaxies are derived from the NASA Sloan Atlas (NSA) catalog[5] (Blanton et al. 2011). After combining the above catalogs and excluding merging galaxies, we have 55 gas-star misaligned star-forming galaxies with available kinematic and stellar population properties, with their mass range being $9.5 < \log M_*/\mathrm{M}_\odot < 10.3$, roughly matching the mass range of our simulated dynamically hot disk galaxies. To make a comparison, we also select a sample (with the same galaxy number as the misaligned sample) of well-aligned star-forming galaxies which have $\Delta\mathrm{PA} < 30°$ in the same mass range. The catalog of these gas-star misaligned galaxies will be released in Chen et al. (in prep.).

We note that our TNG samples explicitly include flatter galaxies (roughly $L_{\mathrm{dev}} < 0.5$ and Sérsic index $n_{\mathrm{Sérsic}} < 2.5$) by design. In comparison, the misaligned MaNGA galaxy sample taken for this study spans a wider range in Sérsic index, with a median of 2.76, spreading from 1 to 6. It is worth noting that dynamically hot disks acquire thicker morphologies along with hotter stellar kinematics after being perturbed by mergers (as can be seen in Fig 14); a thick disk or even spheroidal shape will be a natural morphology in the later evolutionary stages of these galaxies, which are not investigated directly in this study but are expected to feature the same hot kinematics. We have therefore included all galaxies in this MaNGA sample in our analysis regardless of their Sérsic index, in order to increase the sample size. We have checked and confirmed that the distribution of the misalignment angle for the adopted MaNGA galaxy sample does not show dependence on the Sérsic index. To make a direct comparison with MaNGA samples, we project our simulated galaxies (NDs, HDs, and CRs) along the X-axis of the simulation box (equivalent to projecting randomly) and re-calculate the relative parameters (e.g. the V_*/σ_* profiles and stellar ages in given apertures).

In Fig. 16, we present the V_*/σ_* profiles of both MaNGA and TNG (X-projection) samples. As can be seen, MaNGA normal and misaligned samples show similar V_*/σ_* profiles as TNG NDs and HDs+CRs, respectively. Besides, the misaligned star-forming galaxies in MaNGA appear to have lower V_*/σ_* at any radius than their normal galaxy counterparts, indicating the weaker coherent rotation in misaligned MaNGA galaxies, consistent with the kinematic feature of HDs and CRs in the IllustrisTNG Simulation. We note that due to the random projections for the MaNGA and TNG samples, the V_*/σ_* is on average lower than that in Fig. 9 (evaluated from the edge-on projection) at the same radius.

Apart from the similar kinematic feature in MaNGA misaligned star-forming galaxies and TNG dynamically hot star-forming disks (including HDs and CRs), we further demonstrate the connection of these two kinds of galaxies from the other two aspects (i.e. the morphology and the stellar population). We present, in the left panels of Fig. 17, the distributions of galaxy size and Δ log Age as a function of ΔPA for MaNGA misaligned (red) and normal (blue) galaxies. For these MaNGA samples, galaxy size is quantified by the 2D effective radius R_e and Δ log Age is the age difference between two apertures with radii $0.5R_e$ and R_e (negative Δ log Age means that stellar populations in the galaxy center are younger than at the outskirts). As can be seen, MaNGA samples show decreasing trends for log R_e and Δ log Age towards high ΔPA. More specifically, the misaligned star-forming galaxies ($\Delta\mathrm{PA} > 30°$) in MaNGA are obviously of smaller sizes, and have younger stellar populations in their central regions (Δ log Age < 0), reflecting recent star-formation happening therein. These results for MaNGA galaxies are all consistent with the results for the TNG samples (HDs+CRs vs. NDs), which are shown in the right panels. We note here that for the TNG samples, galaxy size is approximated by the half stellar mass radius, R_{hsm}, ΔPA is approximated by $\phi_{\mathrm{Gas-STR}}$ (see Section 3.2 for definition), and due to the spatial resolution limitation, Δ log Age is calculated within apertures with radii R_{hsm} and $2R_{\mathrm{hsm}}$. Besides, HDs, CRs, and NDs in the IllustrisTNG Simulation are divided by orbital fractions (rather than $\Delta\mathrm{PA} = 30°$ used in MaNGA), and as a result, the ΔPA distributions of TNG dynamically hot disks and their normal counterparts are not so well separated as the MaNGA samples.

Despite the slight difference of parameters used in MaNGA and TNG, we can still confirm that the misaligned star-forming galaxies in MaNGA show features in kinematics, morphology, and stellar populations that are all consistent with the dynamically hot star-forming disk galaxies (HDs and CRs) in the IllustrisTNG Simulation, strongly suggesting that these misaligned star-forming MaNGA galaxies are likely to be the real-world counterparts of HDs and CRs in IllustrisTNG. We also predict that the HI disk morphologies of these gas-star misaligned galaxies would be thicker, more

[5] http://nsatlas.org/data

Table 2. The *average* number of mergers since $z = 1$ per galaxy within different galaxy samples of HDs, CRs, and NDs. See Section 4 for definitions of $\theta_{\rm orb}$, μ, and $f_{\rm g}$.

	HDs	CRs	NDs
$\theta_{\rm orb} \geqslant 90°$	0.62 (24%)	0.75 (57%)	0.50 (14%)
$\theta_{\rm orb} < 90°$	1.97 (76%)	0.57 (43%)	3.03 (86%)
$\mu \geqslant 0.01$	1.19 (46%)	0.51 (39%)	1.00 (28%)
$\mu < 0.01$	1.40 (54%)	0.81 (61%)	2.53 (72%)
$f_{\rm g} \geqslant 0.1$	1.32 (51%)	0.92 (70%)	2.11 (60%)
$f_{\rm g} < 0.1$	1.27 (49%)	0.40 (30%)	1.42 (40%)
Total	2.59	1.32	3.53

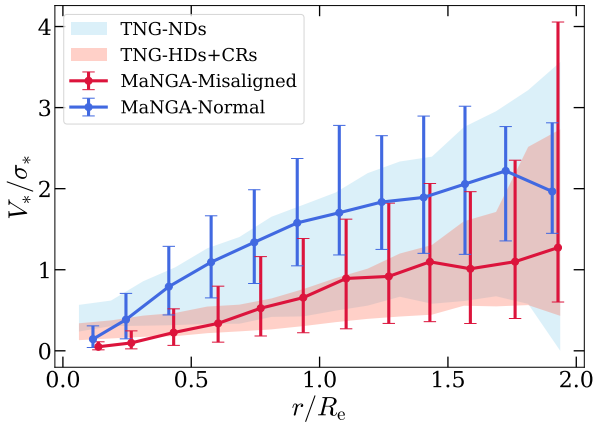

Figure 16. The V_*/σ_* radial profiles ($0-2R_{\rm e}$) of normal (blue) and misaligned (red) samples in MaNGA with the error bars indicating the range from the 16th to the 84th percentiles (1σ). The shaded regions indicate the 1σ ranges of the V_*/σ_* radial profiles ($0-2R_{\rm e}$) for NDs (blue) and the combination of HDs and CRs (red).

concentrated and less well established (as shown by Fig. 5), and that the newly formed stars co-rotate with the existing (counter-rotating) gaseous disk. In particular, for large-angle gas-star misaligned galaxies (that correspond our counter-rotating galaxies), the spin directions of their youngest stellar populations are expected to line up with the cold gas, with both being opposite to that of the older populations in these systems. This should also be reflected in the kinematic maps of H_α, HI, and stars.

6 CONCLUSIONS AND DISCUSSION

In this study, we investigate the nature and origin of (lower-mass) dynamically hot but still actively star-forming disk galaxies in the IllustrisTNG Simulation. These galaxies are selected according to their star-formation activities, stellar morphologies as well as stellar orbital fractions (see Section 2.2). In particular, we identify two subsets of these dynamically hot systems, i.e., hot disk (HD) galaxies and counter-rotating (CR) galaxies (see Fig. 1 and Fig. 2). Our main conclusions are:

(i) Dynamically hot star-forming disk galaxies show smaller sizes (and as a result, higher surface stellar mass densities), thicker morphologies (higher $(c/a)_*$, $(c/a)_{\rm gas}$, and $L_{\rm dev}/L_{\rm tot}$, see Fig. 3, 4, and 5), more centrally-concentrated on-going star-formation (see Fig. 11) and as a result, larger age gradients towards younger stellar populations in the center than at the outskirts (see Fig. 12), in comparison to their normal disk counterparts.

(ii) Dynamically hot star-forming disk galaxies show a common feature of hosting kinematically misaligned gas and stellar disks (see Fig. 6 and Fig. 7), which show weaker coherent rotations and markedly smaller spins than their normal star-forming disk counterparts (see Fig. 8, 9, and 10).

(iii) Galactic interactions and mergers may have played a leading role in the formation of the dynamically hot configurations (see Table 2 and Section 4.4 for details): CRs experienced the least frequent mergers – on average 1.32 mergers per galaxy between $0 \leqslant z \leqslant 1$, among which 57% (w.r.t 14% for NDs and 24% for HDs) showed retrograde merger orbits and 70% (w.r.t. 60% for NDs and 51% for HDs) are gas-rich events; HDs experienced on average 2.59 mergers per galaxy (within the same redshift range), and nearly half of them (46%, w.r.t. 39% for CRs and 28% for NDs) are high mass-ratio events. In comparison, their normal disk counterparts experienced the most frequent mergers – 3.52 mergers per galaxy, however retaining disk morphology and cold kinematics. We emphasize that retrograde mergers as well as larger-mass ratio mergers are primarily responsible to the subsequent build-up of disk thickness and hot/counter-rotating orbits in these galaxies (see Figs. 14 and 15). This is similar to the situation at the more massive end for early-type galaxies for which such mergers play a key role in the formation of slow-rotators during binary mergers (Bois et al. 2011; similar studies also see Martig et al. 2009 and Hoffman et al. 2010). Observational connections between counter-rotating galaxies and retrograde mergers have long been found, such as for NGC 3593, NGC4550 and NGC4191 (Coccato et al. 2013, 2015). In contrast, a correspondence between active AGN feedback and the emergence of dynamically hot disks in these galaxies is not readily evident (also see Khoperskov et al. 2021). We stress that being dynamically hot appears largely as a transient state related to mergers and other galaxy interactions, rather than arising as an age-dependent evolutionary phase of star-forming disk galaxies.

(iv) Gas-star misaligned star-forming galaxies from the MaNGA observations show features in morphology, kinematics and stellar populations that are consistent with the dynamically hot star-forming disks from the TNG simulation. In particular, they are also found to have weaker (co-)rotation and younger stellar populations in galaxy centers than at the outskirts (see Fig. 16 and Fig. 17), indicating that these gas-star misaligned star-forming galaxies are the

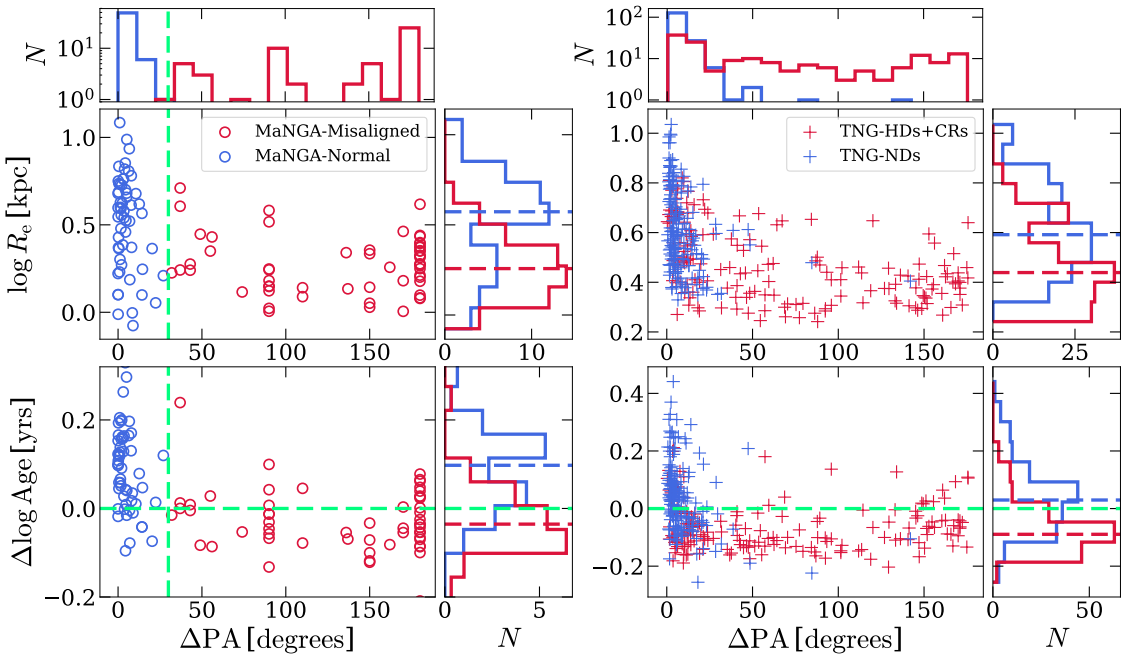

Figure 17. Distributions of galaxy size (top panels) and the age difference between two different apertures (Δ log Age, bottom panels) as a function of ΔPA (see Section 5 for definition) of MaNGA (left panels) and TNG (right panels) samples. For MaNGA samples, galaxy size is quantified by the 2D effective radius R_e and Δ log Age is calculated within two apertures with radii $0.5R_e$ and R_e; for TNG samples, galaxy size is approximated by the half stellar mass radius (R_{hsm}), ΔPA is approximated by $\phi_{Gas-STR}$ (see Section 3.2 for definition), and due to the spatial resolution limitation, Δ log Age is calculated within apertures with radii R_{hsm} and $2R_{hsm}$. MaNGA misaligned and normal samples (see Section 5 for definitions) are indicated by red and blue circles, respectively; the dynamically hot samples (including HDs and CRs) in TNG are indicated by red plus symbols and NDs are indicated by blue symbols. The green dashed vertical lines in the left panels represent ΔPA = 30°, which is the classification criterion of misaligned and normal sample in MaNGA. The green dashed horizontal lines in the bottom panels indicate Δ log Age = 0, below which galaxies are younger in the center than in the outer parts. The histograms indicate the distributions of ΔPA (in the top of the figure) and the investigated properties (log R_e and Δ log Age, to the right of each panel).

real-world counterparts of the dynamically hot TNG disk galaxies examined in this study. In addition, we also predict that the HI disk morphologies in these systems should be thicker, more concentrated and less well established, and that the newly formed stars co-rotate with the existing (counter-rotating) gaseous disk. It is worth noting that in the study of Khoperskov et al. (2021), 90% of counter-rotating stars were found to form in-situ from counter-rotating gaseous disks. We propose for large-angle gas-star misaligned galaxies (that correspond our counter-rotating galaxies), the kinematic maps of H_α, HI, and stars should reveal coherent rotations of the youngest stellar populations and the cold gas, both of which are spinning in the opposite direction with respect to the bulk stellar populations in these systems.

6.1 Minorities in a bigger picture

Star-forming and rotation-supported disk galaxies manage to maintain higher spin than their dynamically hot counterparts. The former dominate in number among today's actively star-forming galaxies, while the latter – systems that possess a good portion of non-corotating stellar components, such as the hot disks and counter-rotators in this study – are only minorities. This is not something that should be taken for granted. It is interesting to put this fact into a larger context and contemplate how this could happen given different processes that determine a galaxy's spin today.

For a given galaxy/halo, the initial tidal field within its Lagrangian region serves as a cosmic spindle machine built upon the filamentary skeletons connected at joints, where flows of gas and dark matter, as well as galaxies/halos eventually meet. On the one hand, such a field provides the galaxy, during the linear growth era, with its initial angular momentum originating from large scale structure torques, which, during the subsequent gravitational collapse and star formation, spins up the gas content and builds up a rotational stellar disk.

On the other hand, the large-scale tidal field to a certain degree also maps out some initial passage ways to numerous galaxy merger events, in particular major mergers, which transfer their coherent orbital angular momenta to the galaxy/halo and further spin it up during such events (Vitvitska et al. 2002; Deason et al. 2011; Rodriguez-Gomez et al. 2017). Note that the Lagrangian region (at the halo's turnaround) in fact already includes most of the structures that would later-on merge into the system (Liao et al. 2018). In this sense, the initial and large-scale tidal field has pre-wired the co-rotating and well-aligned merger/accretion events, and thus predetermines a dominant population of rotational disk galaxies in the first place (see also Rodriguez-Gomez et al. 2017, fig. 10).

Mergers that happen later on, most frequently being minor/mini mergers, and in particular those that involve more massive galaxies, can then be significantly affected by local and internal torques. On top, there are statistical effects from multi-body interactions that induce randomness. As a consequence, these merger trajectories gradually lose memory of the larger-scale tidal field. In-coming

structures, either in form of surviving subhalos and satellite galaxies, or being tidally stripped and smoothly accreted to the galaxy, can significantly alter the host system spin with their in-coming orbit angular momenta (like the CRs and HDs in this study), as well as contribute to the internal torque and induce gravitational instabilities, affecting the subsequent dynamical evolution of the host system. The remnants can also serve as a low-angular momentum reservoir of accreted ex-situ stars. All of the above could reduce the overall angular momentum budget, and induce hot configurations in stellar dynamics (Vitvitska et al. 2002; Zjupa & Springel 2017; Rodriguez-Gomez et al. 2016, 2017).

Apart from galaxy mergers and merging remnants, which all serve as an external source for changing a galaxy's spin, the internal structures and processes of a galaxy can also have an effect. Gravitational instabilities induced by bars or other high-order density moments make stars and gas lose their angular momenta and sink to the centers of galaxies. Energy and momentum feedback from stellar evolution or super-massive black hole growth, which do not directly affect existing stellar populations, can however change/destroy spin carried by cold gas flowing into the galaxy, leaving imprints on the kinematics of the subsequent generation of stars. Such effects can be more important for higher-mass galaxies, which are investigated in a parallel work to this study (Lu et al., in prep).

So what is the answer to the question why there cannot be as many slow- or non-rotating disks as there are fast-rotating disks *among actively star-forming* galaxies in the Universe? Because once the former type comes into existence – through the above-mentioned catastrophic processes of spin-reduction – not only existing stellar populations but also gas would then quickly (within a dynamical time of $\ll 1$ Gyr) sink to the centers of galaxies, where star-forming activities shoot up, accompanied by super-massive black hole accretion and feedback, both diminishing the cold gas reservoir, whose original angular momentum and coherent motion of accretion are then largely wiped out due to direct consumption, feedback heating and turbulent dissipation. Such systems now have heavily reduced star-formation, if not being completely quenched. This is why active star-formation and a high-spin rotational disk always come hand in hand.

6.2 Transition between phases

It is worth noting that even for a "healthy" rotation supported star-forming disk, there could have been transitional stages during which the cold gas reservoir was nearly used up and where star formation died down temporarily, which is indeed seen in some examples of this study. But not before long, the polluted and ejected hot gas (as a consequence of feedback) from the inner galaxy meets pristine cold gas from the CGM/IGM in the outskirts of the galaxy, once again cooling down and falling back to the inner region, where a new cycle of star-formation starts up again. In most cases, this new round of gas accretion ends up co-rotating with the existing stellar disk, both carrying imprints of the same tidal torque field present on large scales. With time, a healthy rotational star-forming disk thus manages its maintenance.

However, there are also cases where the new gas acquisition is strongly affected by, e.g., galaxy mergers (mainly investigated in this study), internal torques from stellar bars, disturbances from energetic feedback, and dissipation when colliding with opposite streams of gas. All these can significantly reduce the total gas spin and cause kinematic misalignment between gas and stars. Then we are back to the picture described above, followed by central star formation and more energy feedback – a dynamically hot star-forming disk emerges!

It is interesting to note that the ensuing fate of these dynamically hot star-forming disks is in fact variable, in particular, if the newly accreted gas eventually dominates the total gas motion and happens to spin in the opposite direction to the existing stellar disk. As such a system is gravitationally stable, with time more and more counter-rotating stars born in this gaseous environment would accumulate and eventually dominate the total stellar spin of the galaxy. With the total spin flipping its direction (now dominated by the counter-rotating component prior to this moment), what used to be the majority stream of co-rotating stars becomes the counter-rotating minority.

In another extreme case, if the triggered feedback process becomes too vicious, so much so that the gas remains hot over some long cooling time, then star-formation will cease. This is why we also observe a large number of slow- or non-rotating ellipticals with quenched star formation in the Universe today. In a parallel work to this study, we investigate such systems at a higher mass scale (Lu et al. in prep). Notice that in more massive galaxies (in particular for $M_* > 10^{11}\,\mathrm{M}_\odot$), this process is also accompanied by more frequent minor mergers, which are found to play a dominant role in diminishing a galaxy's overall spin and aggravating stellar contraction (Vitvitska et al. 2002; Rodriguez-Gomez et al. 2017). What will happen to these systems? If we would wait long enough, we might see them turn again into shining star-forming disks, just like the rejuvenated disk galaxies at high redshifts, but the present-day slow-down of cosmic structure formation due to dark energy might also prevent this from happening again.

ACKNOWLEDGEMENTS

We acknowledge Drs. Lan Wang, Yougang Wang, and Shihong Liao for useful comments and Min Bao for providing the misalignment angle data of the MaNGA galaxies. We also thank the referee for constructive and insightful suggestions and comments which improved the paper. This work is partly supported by the National Key Research and Development Program of China (No. 2018YFA0404501 to SM), by the National Science Foundation of China (Grant No. 11821303, 11761131004 and 11761141012). JW acknowledges the support from the National Science Foundation of China (Grant No. 11991052). VS acknowledges partial support from the German Science Foundation, DFG (Grant No. 653578).

DATA AVAILABILITY

General properties of the galaxies in the IllustrisTNG Simulation is available from `http://www.tng-project.org/data/`. The rest of the data underlying the article will be shared on reasonable request to the corresponding author.

REFERENCES

Aguado D. S., et al., 2019, ApJS, 240, 23
Algorry D. G., Navarro J. F., Abadi M. G., Sales L. V., Steinmetz M., Piontek F., 2014, MNRAS, 437, 3596
Allgood B., Flores R. A., Primack J. R., Kravtsov A. V., Wechsler R. H., Faltenbacher A., Bullock J. S., 2006, MNRAS, 367, 1781
Balcells M., Stanford S. A., 1990, ApJ, 362, 443
Barnes J. E., Hernquist L., 1996, ApJ, 471, 115

Blanton M. R., Kazin E., Muna D., Weaver B. A., Price-Whelan A., 2011, AJ, 142, 31
Bois M., et al., 2011, MNRAS, 416, 1654
Cappellari M., 2017, MNRAS, 466, 798
Cappellari M., Copin Y., 2003, MNRAS, 342, 345
Cappellari M., Emsellem E., 2004, PASP, 116, 138
Catelan P., Theuns T., 1996, MNRAS, 282, 436
Coccato L., Morelli L., Pizzella A., Corsini E. M., Buson L. M., Dalla Bontà E., 2013, A&A, 549, A3
Coccato L., et al., 2015, A&A, 581, A65
Crocker A. F., Jeong H., Komugi S., Combes F., Bureau M., Young L. M., Yi S., 2009, MNRAS, 393, 1255
Deason A. J., et al., 2011, MNRAS, 415, 2607
Dekel A., Birnboim Y., 2006, MNRAS, 368, 2
Dekel A., Birnboim Y., 2008, MNRAS, 383, 119
Dolag K., Borgani S., Murante G., Springel V., 2009, MNRAS, 399, 497
Doroshkevich A. G., 1970, Astrofizika, 6, 581
Falcón-Barroso J., Sánchez-Blázquez P., Vazdekis A., Ricciardelli E., Cardiel N., Cenarro A. J., Gorgas J., Peletier R. F., 2011, A&A, 532, A95
Falcón-Barroso J., et al., 2017, A&A, 597, A48
Fall S. M., 1983, in Athanassoula E., ed., IAU Symposium Vol. 100, Internal Kinematics and Dynamics of Galaxies. pp 391–398
Fall S. M., Efstathiou G., 1980, MNRAS, 193, 189
Genel S., et al., 2014, MNRAS, 445, 175
Genel S., et al., 2018, MNRAS, 474, 3976
Graham A. W., Janz J., Penny S. J., Chilingarian I. V., Ciambur B. C., Forbes D. A., Davies R. L., 2017, ApJ, 840, 68
Hernquist L., Barnes J. E., 1991, Nature, 354, 210
Hoffman L., Cox T. J., Dutta S., Hernquist L., 2010, ApJ, 723, 818
Hoyle F., 1949, MNRAS, 109, 365
Hunter C., Toomre A., 1969, ApJ, 155, 747
Jin Y., et al., 2016, MNRAS, 463, 913
Katkov I. Y., Sil'chenko O. K., Chilingarian I. V., Uklein R. I., Egorov O. V., 2016, MNRAS, 461, 2068
Kereš D., Katz N., Weinberg D. H., Davé R., 2005, MNRAS, 363, 2
Khoperskov S., et al., 2021, MNRAS, 500, 3870
Krajnović D., Cappellari M., de Zeeuw P. T., Copin Y., 2006, MNRAS, 366, 787
Li S.-l., et al., 2021, MNRAS, 501, 14
Liao K., Ding X., Biesiada M., Fan X.-L., Zhu Z.-H., 2018, ApJ, 867, 69
Lu S., et al., 2020, MNRAS, 492, 5930
Marinacci F., et al., 2018, MNRAS, 480, 5113
Martig M., Bournaud F., Teyssier R., Dekel A., 2009, ApJ, 707, 250
Mo H. J., Mao S., White S. D. M., 1998, MNRAS, 295, 319
Naiman J. P., et al., 2018, MNRAS, 477, 1206
Nelson D., et al., 2015, Astronomy and Computing, 13, 12
Nelson D., et al., 2018, MNRAS, 475, 624
Nelson D., et al., 2019a, Computational Astrophysics and Cosmology, 6, 2
Nelson D., et al., 2019b, MNRAS, 490, 3234
Peebles P. J. E., 1969, ApJ, 155, 393
Pillepich A., et al., 2018, MNRAS, 475, 648
Pillepich A., et al., 2019, MNRAS, 490, 3196
Pizzella A., Corsini E. M., Vega Beltrán J. C., Bertola F., 2004, A&A, 424, 447
Pizzella A., Morelli L., Coccato L., Corsini E. M., Dalla Bontà E., Fabricius M., Saglia R. P., 2018, A&A, 616, A22
Planck Collaboration et al., 2016, A&A, 594, A13
Puerari I., Pfenniger D., 2001, Ap&SS, 276, 909
Rodriguez-Gomez V., et al., 2015, MNRAS, 449, 49
Rodriguez-Gomez V., et al., 2016, MNRAS, 458, 2371
Rodriguez-Gomez V., et al., 2017, MNRAS, 467, 3083
Roškar R., Debattista V. P., Brooks A. M., Quinn T. R., Brook C. B., Governato F., Dalcanton J. J., Wadsley J., 2010, MNRAS, 408, 783
Sánchez-Blázquez P., et al., 2006, MNRAS, 371, 703
Sánchez S. F., et al., 2018, Rev. Mex. Astron. Astrofis., 54, 217
Schaye J., et al., 2015, MNRAS, 446, 521
Springel V., 2010, MNRAS, 401, 791
Springel V., White S. D. M., Tormen G., Kauffmann G., 2001, MNRAS, 328, 726
Springel V., et al., 2018, MNRAS, 475, 676
Starkenburg T. K., Sales L. V., Genel S., Manzano-King C., Canalizo G., Hernquist L., 2019, ApJ, 878, 143
Stoughton C., et al., 2002, AJ, 123, 485
Thakar A. R., Ryden B. S., 1996, ApJ, 461, 55
Tohline J. E., Durisen R. H., 1982, ApJ, 257, 94
Vitvitska M., Klypin A. A., Kravtsov A. V., Wechsler R. H., Primack J. R., Bullock J. S., 2002, ApJ, 581, 799
Vogelsberger M., Genel S., Sijacki D., Torrey P., Springel V., Hernquist L., 2013, MNRAS, 436, 3031
Vogelsberger M., et al., 2014a, MNRAS, 444, 1518
Vogelsberger M., et al., 2014b, Nature, 509, 177
Wang J., Koribalski B. S., Serra P., van der Hulst T., Roychowdhury S., Kamphuis P., Chengalur J. N., 2016, MNRAS, 460, 2143
Westfall K. B., et al., 2019, AJ, 158, 231
White S. D. M., 1984, ApJ, 286, 38
Xu D., Springel V., Sluse D., Schneider P., Sonnenfeld A., Nelson D., Vogelsberger M., Hernquist L., 2017, MNRAS, 469, 1824
Xu D., et al., 2019, MNRAS, 489, 842
Zavala J. A., et al., 2015, MNRAS, 452, 1140
Zhu L., van de Ven G., Méndez-Abreu J., Obreja A., 2018, MNRAS, 479, 945
Zjupa J., Springel V., 2017, MNRAS, 466, 1625
de Vaucouleurs G., 1948, Annales d'Astrophysique, 11, 247
van de Voort F., Davis T. A., Kereš D., Quataert E., Faucher-Giguère C.-A., Hopkins P. F., 2015, MNRAS, 451, 3269